This is the peer-reviewed, final accepted version for American Mineralogist, published by the Mineralogical Society of America.
The published version is subject to change. Cite as Authors (Year) Title. American Mineralogist, in press.
DOI: https://doi.org/10.2138/am-2021-7675. http://www.minsocam.org/

Revision 1 **Word Count: 11241**

Effects of arsenic on the distribution and mode of occurrence of gold during fluid–pyrite interaction: a case study of pyrite from the Qiucun gold deposit, China

He Zhang[1,2], Yuanfeng Cai[1]*, Gang Sha[3], Joël Brugger[4], Allan Pring[2], Pei Ni[1], Gujie Qian[2], Zhenjiao Luo[3], Yang Zhang[1], Wei Tan[5]

[1]State Key Laboratory of Mineral Deposit Research, School of Earth Sciences and Engineering, Nanjing University, Nanjing 210023, China
[2]School of Chemical and Physical Sciences, Flinders University, Adelaide, South Australia 5001, Australia
[3]Herbert Gleiter Institute of Nanoscience, School of Materials Science and Engineering, Nanjing University of Science and Technology, Nanjing 210094, China.
[4]School of Earth, Atmosphere and Environment, Monash University, Clayton, Victoria 3800, Australia
[5]Key Laboratory of Mineralogy and Metallogeny, Guangzhou Institute of Geochemistry, Chinese Academy of Sciences, Guangzhou 510640, China

ABSTRACT

This paper presents the results of an investigation of the incorporation of Au within pyritic ore from the Qiucun epithermal Au deposit, China. The new data provide insights into the mode of occurrence of Au during fluid–rock interactions within epithermal systems. The distribution and mode of occurrence of Au within arsenian pyrite was investigated using a chemical and structural characterization based approach combining laser ablation inductively coupled plasma mass spectrometry (LA–ICP–MS) trace element analysis, megapixel synchrotron X-ray fluorescence analysis (MSXRF), and atom probe tomography (APT). The resulting data indicate that invisible Au is present at elevated concentrations in the form of a homogeneous solid solution within As-rich pyrite domains, which yields Au concentrations that positively correlate with As. Arsenic-induced lattice defects, such as stacking faults and the expansion of the pyrite

unit-cell, provide evidence of the effect of As on the incorporation of Au into pyrite. The nucleation and crystallization of electrum preferentially occurred at the fluid–pyrite reaction interface, or along fractures and grain boundaries within the pre-existing pyrite. This study indicates that changes in physico-chemical conditions (e.g., temperature, pH, and sulfur fugacity) during fluid-pyrite interactions are key controls on the development of nano- or μm-scale clusters of gold. The systematic compositional and textural observations documented in this study provide new insights into the mechanisms responsible for the different modes of occurrence of Au (ionic versus particulate), and enable us to further understand the processes involved in the formation of Au mineralization.

Keywords: gold; arsenian pyrite; fluid–rock interaction; epithermal gold deposit

INTRODUCTION

Pyrite is one of the most important hosts of Au within Au mineralization, with Au either present as visible (>1000 Å) or "invisible" (<1000 Å) Au. Previous research suggests that the invisible Au in arsenian pyrite is present as either nanoparticles (Au^0) or in the form of solid solution Au^+ incorporated within the pyrite lattice (Aylmore, 1995; Bakken et al., 1989; Filimonova et al., 2020; Fleet et al., 1993; Merkulova et al., 2019; Palenik et al., 2004; Reich et al., 2005; Simon et al., 1999), or in the form of Au_2S-like clusters/inclusions (Filimonova et al., 2020; Pokrovski et al., 2019). Multiple possible mechanisms are thought to control the modes of Au incorporation into arsenian pyrite, with Palenik et al. (2004) and Reich et al. (2005) suggesting that Au solubility is the most important factor. The maximum content of solid solution Au within arsenian pyrite has been defined as a function of As content as follows: $C_{Au} = 0.02C_{As} + (4 \times 10^{-5})$, where

This is the peer-reviewed, final accepted version for American Mineralogist, published by the Mineralogical Society of America.
The published version is subject to change. Cite as Authors (Year) Title. American Mineralogist, in press.
DOI: https://doi.org/10.2138/am-2021-7675. http://www.minsocam.org/

55 C_{Au} and C_{As} represent the concentrations of Au and As within the arsenian pyrite,
56 respectively (Reich et al., 2005). Gopon et al. (2019) suggested that point defects caused
57 by the incorporation of As into the pyrite structure may also facilitate the solid solution
58 incorporation of Au. The diffusion of Au ions within crystals is also an important control
59 on the recrystallization and distribution of Au, as demonstrated by the coarsening of Au
60 nanoparticles into larger size particles as a result of the diffusion of Au through pyrite
61 during *in situ* heating (Reich et al., 2006). The combined action of crystal growth and Au
62 ion surface diffusion may cause the dominance of different modes of Au incorporation,
63 with slow crystal growth inducing the formation of Au nanoparticles by surface diffusion
64 (Fougerouse et al., 2016b). The post-crystallization exsolution of solid solution Au from
65 metastable arsenian pyrite may also occur during post-mineralization metamorphism
66 (Palenik et al., 2004). Finally, fluid-mediated interface coupled dissolution–
67 reprecipitation replacement (ICDR; e.g., Putnis, 2009) is thought to be a common
68 mechanism for the release of trace elements from parental phases or hydrothermal fluids
69 into product phases, in a process that is contemporaneous with changes in the distribution
70 and mode of Au occurrence (Altree-Williams et al., 2015; Fougerouse et al., 2016a;
71 Geisler et al., 2007; Harlov et al., 2011; Li et al., 2018a; Putnis, 2009; Wu et al., 2019a;
72 Xia et al., 2009; Zhao et al., 2009, 2013, 2017).

73 Despite the significant amount of research undertaken on the nature of invisible Au
74 in arsenian pyrite, little is known about the role of As on the incorporation of Au into this
75 mineral. One key variable is the behavior of Au during fluid–rock interactions involving
76 As, and the link between this behavior and whether Au is incorporated into arsenian
77 pyrite in visible or invisible forms. This study presents new megapixel synchrotron-based

X-ray fluorescence (MSXRF) and atom probe tomography (APT) data that provide information on the distribution and modes of occurrence of Au in arsenian pyrite from epithermal Au deposits. These data provide insights into the controls on the different modes of Au incorporation into arsenian pyrite.

GEOLOGICAL SETTING

The Qiucun gold deposit

The Qiucun Au deposit is a low-sulfidation epithermal Au deposit located within the Dehua region of central Fujian Province, southeast China (Fig. 1; Huang et al., 2017; Ni et al., 2018; Zhang et al., 2017). The deposit is hosted by volcanic rocks of the Upper Jurassic Nanyuan Formation and sandstones of the Changlin Formation (Guilin Geology and Mining Limited Company, 2003) and has known reserves of 10 t Au (FIGSR, 2014). The Au mineralization at Qiucun is predominantly hosted by hydrothermal veins and locally developed breccias. The veins are subdivided into chalcedony, pyrite-rich, pyrite-poor, and calcite-bearing subtypes (Ni et al., 2018). The auriferous veins within the deposit at elevations of 712, 742, and 820 m above sea level (ASL) formed at temperatures of 180°C–250°C as determined by the homogenization temperatures of quartz-hosted fluid inclusions (Ni et al., 2018). Fluid inclusion, petrological, and textural evidence suggests that fluid boiling was the key control on Au precipitation within the deposit (Ni et al., 2018). This study used > 100 hand specimens that were collected from auriferous veins from ore bodies at elevations of 712, 742, 772, and 820 m ASL within the Qiucun Au deposit. This study focused on pyrite-rich and chalcedony vein subtypes (Fig. 2a–b), with the two sampled vein subtypes yielding Au grades of 3–11 and > 30 g/t,

This is the peer-reviewed, final accepted version for American Mineralogist, published by the Mineralogical Society of America.
The published version is subject to change. Cite as Authors (Year) Title. American Mineralogist, in press.
DOI: https://doi.org/10.2138/am-2021-7675. http://www.minsocam.org/

101 respectively (Ni et al., 2018). These auriferous veins contain visible Au in the form of
102 electrum closely associated with chalcopyrite and pyrite (Fig. 2c–e). In addition, pyrite in
103 these veins is commonly growth zoned, with inclusion-rich cores and relatively
104 intrusion-free (clean) rims (Fig. 2f). The zoned pyrite contains high concentrations of Au
105 and is the main host of Au within the deposit, indicating they are a valuable source of
106 information on the processes involved in the generation of Au-enriched pyrite during
107 fluid–rock interactions.
108
109 **The Dongyang gold deposit**
110 The Dongyang Au deposit is a recently discovered low-sulfidation Au deposit located
111 near the Qiucun Au deposit (Li et al., 2018b; Xu et al., 2018, 2019; Zhang et al., 2018).
112 The deposit hosts reserves of 22 t of Au at an average grade of 2.83 g/t Au (FIGSR, 2014).
113 The majority of the mineralization is hosted by porphyritic rhyolite and volcanic rocks of
114 the Upper Jurassic Nanyuan Formation (Li et al., 2018b; Xu et al., 2018, 2019; Zhang et
115 al., 2018). The mineralization within the deposit is divided into two main stages (Zhang
116 et al., 2018). The early, reduced stage is associated with arsenopyrite, arsenian pyrite, and
117 marcasite mineralization, whereas the late oxidized stage is associated with Ag minerals
118 and polymetallic sulfides such as pyrite, chalcopyrite, sphalerite, and galena.
119 Microthermometric analysis of fluid inclusions within auriferous quartz–sulfide veins
120 yielded homogenization temperatures of 172°C–217°C (mean of 192°C; Li et al., 2018b).
121 The samples used in this study were taken from drill hole ZK1033 at an elevation of
122 303 m ASL.
123 This study mainly focused on samples from the Qiucun Au deposit, as the geology

and the morphologies, textures, and compositions of minerals within the samples from this deposit are more closely constrained with respect to fluid–rock interactions than the samples from the Dongyang deposit. However, the fact that the pyrite from the Dongyang deposit contains more As (~8 wt%) than those in the Qiucun deposit means the former is critical for the determination of the effects of As incorporation into the pyrite structure, as well as the interpretation of the behavior of Au–As at higher As concentrations.

ANALYTICAL METHODS

Scanning electron microscopy

Cut slabs of the mineralized samples from the Qiucun deposit were embedded in epoxy resin, mounted on 1 mm-thick quartz slides, and polished into ~100 μm-thick thin-sections. The sections were then carbon-coated, and their petrographic textures were characterized using a Zeiss supra 55 scanning electron microscope (SEM) in back-scattered electron (BSE) mode operated at an accelerating voltage of 15 kV. The SEM is also equipped with energy dispersive X-ray spectrometers (EDS) for semi-quantitative chemical analysis to aid mineral identification.

Electron microprobe analysis

The chemical composition of arsenian pyrite was determined using electron microprobe analysis (EMPA) employing a JXA 8230 instrument. The EMPA undertaken during this study used the same thin-sections as for SEM BSE imaging. These sections were re-polished, cleaned in ethanol to remove any oxide layers and impurities from the sample surface, and were then recoated with carbon. Elements, X-ray lines and standards used were: Fe*Kα*/pyrite, S*Kα*/pyrite, As*Lα*/arsenopyrite, Co*Kα*/$(Co,Fe,Ni)_9S_8$,

This is the peer-reviewed, final accepted version for American Mineralogist, published by the Mineralogical Society of America.
The published version is subject to change. Cite as Authors (Year) Title. American Mineralogist, in press.
DOI: https://doi.org/10.2138/am-2021-7675. http://www.minsocam.org/

148 Ni*Kα*/(Co,Fe,Ni)$_9$S$_8$, Sb*Lα*/ Sb$_2$Te$_3$, Ag*Lα*/ Ag$_2$S$_3$. The analyses were undertaken using an
149 accelerating voltage of 15 kV and a beam current of 20 nA. The beam spot diameter was
150 set at 1 μm.
151
152 **Laser ablation inductively coupled plasma mass spectrometry**
153 The concentrations of trace elements within the pyrite analyzed previously by SEM
154 and EMPA were determined using an Agilent 7700x quadrupole ICP–MS instrument
155 coupled to a Photon Machines Excite 193 nm Excimer LA system. The analytical method
156 is similar to that described by Gao et al. (2015). Two pumps (rotary vane and
157 turbo-molecular pumps) were used for the vacuum system. Each analysis used a 40 μm
158 diameter ablating spot with a laser frequency of 8 Hz and laser energy of ~5 mJ per pulse,
159 with data acquired for 40 s after determining the gas blank for 15 s. Calibration was
160 undertaken using USGS GSE-1G (synthetic basaltic glass) and GSC 12744 (pyrite)
161 standards, both of which were analyzed along with unknowns. The ICPMSDataCal
162 software package was used for off-line signal selection, integration, time-drift correction,
163 and quantitative calibration (Liu et al., 2008). The resulting data has a precision of < ±20%
164 for most elements present at > 1 ppm, and < ±10% for the elements present at > 50 ppm.
165
166 **Megapixel synchrotron X-ray fluorescence and atom probe tomography**
167 The distribution of individual elements within the samples from the study area was
168 determined using MSXRF and APT. The As-free quartz slide-mounted ~100 μm-thick
169 polished thin-sections described above were used for MSXRF analysis with X-ray
170 elemental images collected in the Maia 384 (Sync)-HYMOD data acquisition format

before being reduced at the Australian Synchrotron, Melbourne, Australia. The acquired data were analyzed using the CSIRO Dynamic Analysis approach within the GeoPIXE software package, which enables quantitative, true elemental concentration images to be unmixed from the generally complex PIXE/SXRF energy spectra. More details of the analytical procedures are given in Fisher et al. (2014) and Li et al. (2016). The resulting quantified images can be directly interrogated to determine the concentrations of all detected elements in portions of the images using the interactive GeoPIXE II software. Although the Au Lα emission line is partly obscured by the intense As Kα line (Merkulova et al., 2019), minor peaks and shoulders within the spectra are positively correlated to Au concentrations due to the full profile fitting approach (Fisher et al., 2014). The presence of the Au (Lα) peak was identified on the shoulder of the As (Kα) peak (Fisher et al., 2014), enabling the generation of Au distribution maps by removal of the interfering As (Kα) overlap.

Atom probe microscopy provides three-dimensional (3D) maps that indicate the distribution of individual atoms (e.g., Fougerouse et al., 2016b; La Fontaine et al., 2017; Wu et al., 2019b). Regions of interest (ROI) for atom probe specimens were selected from pyrite domains with high concentrations of As and Au and electrum (Au–Ag alloy; Fig. 3), respectively. Prior to analysis, three needle-shaped APT specimens were prepared by electro-polishing combined with the extraction of the ROI from the sample surface using an Auriga focused ion beam scanning electron microscope (FIB-SEM). The APT analysis was undertaken using a LEAP4000XSi atom probe equipped with a picosecond pulse ultraviolet laser (355 nm; spot size < 4 μm) at the Herbert Gleiter Institute of Nanoscience, Nanjing University of Science and Technology, Nanjing, China. This

194 analysis used a specimen temperature of 40 K, a 60 pJ laser pulse energy, and a 200 kHz
195 laser frequency, with a 0.4%–0.8% detection rate, 2×10^{-11} torr analysis chamber vacuum
196 setting, and 14–40 M total ion collection. The data were reconstructed and visualized
197 using the Integrated Visualization and Analysis Software (IVAS 3.6.8) developed by
198 Cameca Scientific Instruments. The efficiency of the detector is about 55% and the
199 instrument has a trace element detection sensitivity of ~50 ppm.
200

201 **Electron backscatter diffraction, transmission electron microscopy, and X-ray**
202 **powder diffraction**

203 The structural characterization of arsenian pyrite was undertaken using electron
204 backscatter diffraction (EBSD), transmission electron microscopy (TEM), and X-ray
205 powder diffraction (XRD). Pyrite EBSD orientation maps were acquired using an Oxford
206 Instruments HKL Nordlys II EBSD detector coupled to a FEI Quanta 450 field emission
207 gun SEM at the China University of Geosciences, Wuhan, China. This analysis was
208 undertaken in automatic mode using a step size of 2 μm and an operating voltage of
209 15 kV.

210 Six ~8 × 3 μm TEM foils from the high Au and As areas of pyrite were prepared
211 using FIB-SEM on a Zeiss Auriga Compact instrument at the Institute of Geology and
212 Geophysics, Beijing, China. These TEM foils were extracted using an Omniprobe
213 AutoProbe200 micromanipulator before being attached to a copper TEM grid with
214 support film and being thinned down to a suitable thickness range (50–100 nm) at various
215 accelerating voltages and beam currents. These foils were stored in an anoxic glove box
216 filled with N_2 gas prior to analysis. They were imaged using a FEI Tecnai F20 TEM at

Nanjing University, and a Thermo Fisher Titan Themis 80-200 (equipped with a probe corrector) at Adelaide University. Both instruments were operated at 200 kV for bright-field (BF) TEM observations, selected-area electron diffraction (SAED), high-angle annular dark-field (HAADF) observations, and energy-dispersive X-ray analyses (~1 wt% detection limit). The latter two observations and analyses were conducted under scanning TEM (STEM) mode. The calibration was performed on the basis of the ring pattern of the standard Au specimen. Elemental mapping was performed under scanning TEM mode using an Oxford Aztec software.

Individual arsenian pyrite grains separated from crushed mineralized samples were milled in acetone prior to XRD analysis. This approach used pyrite spiked with 50 wt% corundum and employed a Bruker D8 Advance Eco X-ray diffractometer using Co$K\alpha$ radiation (λ = 1.7902 Å) generated at 35 kV and 28 mA at Flinders University. The cell parameters were determined using a full-pattern fitting Rietveld method (Hunter, 1998; Rietveld, 1969) with the aid of TOPAS version 6.0. A Pseudo-Voigt function and a fifth-order Chebychev polynomial were used to model peak shapes and background, respectively. Zero shifts were taken from refinements of the powder diffraction pattern for the spiked corundum powders and the crystal structural data for the refinement were taken from the Crystallography Open Database (pyrite code: 9000594; corundum code: 1000017).

RESULTS

Textures and compositions of arsenian pyrite: SEM, EMPA, and LA-ICP-MS data

The textural characteristics of the arsenian pyrite from the Qiucun deposit were

240 determined at the micrometer and sub-micrometer scales using SEM imaging (Fig. 3).
241 The pyrite is either subhedral or anhedral and contains other metal-bearing grains (e.g.,
242 electrum; Fig. 3), either in the form of micrometer- or sub-micrometer-sized inclusions
243 (Fig. 3) or as fracture-filling veins (Fig. 3a, c, f).

244 EMPA indicates that the pyrite within the deposit is As-rich (up to ~5 wt%; Appendix
245 Table S2). Arsenic is unevenly distributed throughout the pyrite at the μm-scale and is
246 concentrated in either zones or patches (Fig. 3). The As-rich domains within the pyrite
247 contain 0.1–5 wt% As, with As-deficient domains containing < 0.1 wt% As (Fig. 3;
248 Appendix Table S2). Local interfaces between As-rich and -deficient pyrite domains
249 (Fig. 3) host the majority of the electrum. Electrums also occur as sub-micrometer-sized
250 spheroidal inclusions (Fig. 3c), or as fracture-filling veins (Fig. 3a, c, f) within the
251 As-deficient pyrite domains. These features suggest the importance of metasomatic
252 processes associated with the interaction between As-rich hydrothermal fluids and
253 pre-existing pyrite in controlling As and Au distribution.

254 The trace element analysis of the As-rich zones yielded an average Au concentration
255 of 18 ppm (Appendix Table S1). There is a strikingly positive correlation between the
256 invisible Au and As within pyrite ($R^2 = 0.79$; Figs. 4 and S1). These data suggest that Au
257 values lie below the solubility limit predicted by Reich et al. (2005), consistent with Au
258 being incorporated via solid solution in these As-rich pyrites (Fig. 4). The LA–ICP–MS
259 analysis also yielded mean concentrations of 283(28) ppm Cu, 97(10) ppm Ag, 96(10)
260 ppm Sb, 16(3) ppm Te, 4(1) ppm Se, and 476(48) ppm Pb. The presence of coexisting
261 elemental anomalies within these data, including for analyses QCPY-21 (2006(200) ppm
262 Cu, 542(54) ppm Ag, 358(36) ppm Sb, and 455(46) ppm Pb) and QCPY-32 (559(56)

ppm Ag, 344(34) ppm Te, and 1360(136) ppm Pb; Appendix Table S1), suggest that the As-rich pyrite domains may contain Cu–Ag–Sb–Pb–Te-rich zones or clusters.

MSXRF elemental mappings

The MSXRF red–green–blue (RGB) image shows the distribution of K, Au, and As within samples from the study area (Fig. 5), with K used as a proxy for sericite (Fig. S2). Pyrite is shown in blue (As) as the pyrite in the study area commonly contains elevated concentrations of As (Fig. 3). The pyrite contains cyclical, oscillatory, and irregular As zonation (Fig. 5). The oscillatory zones are of particular interest and usually record pulsed As-rich fluid flow and/or changes in the prevailing physico-chemical conditions, both of which can affect the incorporation of As into pyrite. Auriferous minerals (green) are also visible in the RGB image (Fig. 5), with SEM imaging and EMPA indicating that these minerals are electrum. The electrum within the pyrite is spatially associated with the distribution of As, where the majority of electrum is located at the interface between As-rich and -deficient pyrite domains. The high penetration ability of hard X-rays during MSXRF and the associated ability to measure subsurface features in samples (e.g., for AuLα (9.712 keV), ~56% of characteristic X-ray escape from a depth of 10 μm; del Real et al., 2019; Etschmann et al., 2010; Fisher et al., 2014; Li et al., 2016; Sutton et al., 2002) mean that those metal-bearing inclusions (Fig. 3a, c, d, f) within the As-deficient pyrite interior most likely were associated with As-rich sections that are not able to be identified using SEM. In addition, the zoned distribution of invisible Au within pyrite is readily visible in the MSXRF Au maps (Fig. 5a–c), with the coupled distribution of invisible Au and As identified within pyrite.

EBSD orientation mapping

EBSD mapping indicates that the most pyrite crystals (Fig. 6a) are actually an aggregate of smaller crystals in different crystallographic orientations, as indicated by the random distribution of pyrite grain orientations within the pole figures (Figs. 6b and S3). A comparison between the colored EBSD map and BSE map indicates that the incorporation of As does not cause variations in the crystallographic orientation of the pyrite. It is also worth noting that the electrum is located along subgrain boundaries with grain misorientations of > 5°.

XRD patterns of arsenian pyrite

Unit cell parameters retrieved from the Rietveld refinement of Powder XRD patterns for arsenian pyrite (5.41887(10) Å; Fig. S4) are significantly larger than those reported for As-free pyrite in previous studies (e.g., 5.4151 Å, Wu et al., 2004; 5.4160 Å, Li et al., 2018c). The Rp, Rwp, and GOF values of the Rietveld refinement are 1.89, 1.39, and 2.87, respectively.

TEM study

The HAADF-STEM analysis of the foil was extracted from the ROI with ~4 wt% As and ~40 ppm Au (Fig. 7a) identified very few bright nanoparticles with higher average atomic masses (Z) than the As-pyrite matrix (Fig. 7b–c). These nanoparticles range in size from 20–200 nm and have well defined boundaries with the As-pyrite matrix. Combining EDS and SAED analyses with this HAADF-STEM analysis identified a Ag–Sb phase and chalcopyrite, but provided no evidence of any auriferous phases (Figs. 7d–e

This is the peer-reviewed, final accepted version for American Mineralogist, published by the Mineralogical Society of America.
The published version is subject to change. Cite as Authors (Year) Title. American Mineralogist, in press.
DOI: https://doi.org/10.2138/am-2021-7675. http://www.minsocam.org/

and S5. The absence of Au nanoparticles throughout the As-rich pyrite matrix is consistent with the incorporation of all of the invisible Au within this sample by solid solution.

Crystal–chemical considerations suggest that the incorporation of As in the pyrite structure should generate significant numbers of defects as a result of different effective ion radii (e.g., Cook and Chryssoulis, 1990; Dubosq et al., 2019; Fleet and Mumin, 1997; Liang et al., 2013; Simon et al., 1999). The SAED patterns generated during this study indicate that the As-pyrite is highly crystalline (Fig. 7d), but the HRTEM imaging identified local crystal misorientations with d-spacings of 0.19 and 0.31 nm associated with the {220} and {111} planes of pyrite, respectively (Fig. 7f–h).

A FIB-cut was also extracted from an area containing the interface between As-deficient and -rich pyrite domains (Fig. 8). The epitaxial growth of As-pyrite is evidenced by a comparison of two patterns that provide evidence of consistent orientation on both sides of the interface in a [0 1 $\bar{1}$] projection (Fig. 8b–c). In addition, the unit-cell parameters of both two pyrite domains were obtained using the UnitCell program (Holland and Redfern, 1997) on the basis of the SAED patterns, with As-induced expansion identified by differences in face intercepts of As-rich (5.46(2) Å) and -deficient (5.42(2) Å) pyrite domains.

A third FIB-cut was extracted from highly As-enriched (~8 wt% As; Fig. 9) pyrite from the Dongyang Au deposit to further investigate the effect of As on the pyrite structure and provide more information on fluid–rock interface features. The combined HAADF imaging and EDS data indicate the presence of a sharp interface between As-rich and -deficient pyrite domains in this sample. Fine layers of arsenopyrite or

marcasite-type phases have been previously identified within arsenian pyrite (e.g., Dodony et al., 1996; Simon et al., 1999). Our HAADF–STEM images (Fig. 10) reveal that stacking faults at the periphery of this interface are parallel to one another, are filled with galena nanoparticles, and terminate at the interface in a [0 1 $\bar{1}$] projection. This atomic arrangement suggests the presence of a planar fault parallel to the (2 0 0) plane with local narrowing (0.23 nm) and widening (0.32 nm) of lattice rows (Fig. 10e). There is no obvious lattice mismatch at the interface, but instead this area contains long-range ordered atomic arrangements on both sides of the boundary (Fig. 10d–e). In addition, local highly-crystalline As-rich and -deficient pyrite domains are present (Fig. 10f–g), with the As-rich domains characterized by a larger d-spacing than the As-deficient ones.

APT study

Three needle-shaped specimens were prepared using FIB-SEM with two specimens extracted from As-rich pyrite domains (S1 and S2; 20–30 ppm Au) and the final one extracted from electrum for Au peak calibration (S3; Fig. 3). We only describe the results for S1, as the data for S1 and S2 are very similar. The APT data suggest that the analyzed region contains 1.57 at% As, but no significant Au levels (Appendix Fig. S6; Appendix Table S4). The detection limit for Au was estimated to be 60 ppm with the given mass spectrum background level, indicating that a Au concentration of ~30 ppm would only yield detectable Au if the Au present was in the form of nanoparticles or highly enriched domains (Appendix Fig. S6; Appendix Table S4). Although the concentrations of Cu, Pb, As, Sb, Ge, and Se are generally homogeneous (Fig. 11), the upper end of the Cu map suggests the presence of Cu-rich clusters. The further analysis of these clusters involved

This is the peer-reviewed, final accepted version for American Mineralogist, published by the Mineralogical Society of America.
The published version is subject to change. Cite as Authors (Year) Title. American Mineralogist, in press.
DOI: https://doi.org/10.2138/am-2021-7675. http://www.minsocam.org/

the creation of an isoconcentration surface (i.e., an isosurface) at the location with a combined Cu, Se, and Pb concentration of 0.2 at% (Fig. 12). The enrichment of Cu and Sb in this area is identified by proxigrams across the isosurface (Fig. 12c), representing the presence of atomic clustering. However, there is no obvious atomic clustering in other areas, with a nearest neighbor analysis finding no statistical evidence for the clustering of Cu, Pb, As, Sb, Ge, and Se (Fig. 13). This indirectly suggests that the invisible Au within these samples is present in a homogeneous solid solution form rather than as nanoparticles.

DISCUSSION

Incorporation of arsenic within arsenian pyrite

Arsenic is one of the most significant impurities in pyrite and is thought to be incorporated into the pyrite structure by the substitution of As^{-} for S^{-} (e.g., Blanchard et al., 2007; Deditius et al., 2008; Fleet and Mumin, 1997; Liang et al., 2013; Pals et al., 2003; Reich et al., 2005; Savage et al., 2000; Simon et al., 1999; Zachariáš et al., 2004), by substituting for Fe^{2+} in the form of As^{3+} (Deditius et al., 2008) or As^{2+} (Qian et al., 2013), or by incorporation as amorphous nanoparticles (As^{0}; Deditius et al., 2009). Plotting the pyrite from the study area in an Fe–S–As (at%) ternary diagram provides evidence of whether As is substituting for S and/or Fe. Here, $As^{3+/2+}$-pyrite would define a trend parallel to the Fe–As join, indicative of the presence of As within octahedral Fe sites, whereas As^{1-}-pyrite would plot close to the As–S join, indicating the presence of As within the octahedral S site (Deditius et al., 2008; Liang et al., 2013). The As-pyrite from the study area defines a dispersed trend parallel to the As–S join in the Fe–S–As (at%)

This is the peer-reviewed, final accepted version for American Mineralogist, published by the Mineralogical Society of America.
The published version is subject to change. Cite as Authors (Year) Title. American Mineralogist, in press.
DOI: https://doi.org/10.2138/am-2021-7675. http://www.minsocam.org/

ternary diagram (Fig. 14a), suggesting that As is substituting for S within the pyrite structure (Fig. 14a). The EMPA-determined concentrations of As and S within the pyrite also strongly negatively correlate ($R^2 = 0.92$), again suggesting that As is substituting for S (Fig. 14b).

Savage et al. (2000) demonstrated that As substitutes S with significant As–As clustering in the As-pyrite samples from tailings of the Clio Mine of the Mother Lode Gold District, with the formation of As–As pairs being energetically favorable on the basis of the thermodynamic calculations by Manceau et al. (2020). In contrast, Filimonova et al. (2020) reported the absence of As–As clustering in the synthetic and natural As-pyrite samples from the Samolazovskoe Au-sulfide deposit and the Vorontsovka Carlin-type deposit. The homogeneous distribution of As atoms (or ions) within the As-pyrite matrix in our samples from the study area was identified through APT mapping and nearest neighbor distribution analysis (Figs. 11–13). Arsenic-induced expansion of pyrite structure was evident, with the cell parameter (5.41887(10) Å) of As-pyrite derived by Rietveld refinement of powder XRD patterns (Fig. S4) being larger than those reported for As-free pyrite in previous studies (e.g., 5.4151 Å, Wu et al., 2004; 5.4160 Å, Li et al., 2018c). The expansion was also identified based on the SAED patterns (Fig. 8) where the cell parameter (5.46(2) Å) of the As-rich pyrite domain (~2 wt% As) was larger than the one (5.42(2) Å) of the As-deficient domain (< 0.1 wt% As; Table S3).

Controls on arsenic-rich zones in pyrite

The precipitation of As-pyrite on the surface of pre-existing As-free pyrite has been

401 identified during previous studies (e.g., Wu et al., 2019b). The pyrite shown in Figs. 3
402 and 5 contains cyclical, oscillatory, and irregular As-rich zones. These zones can form in
403 various ways that can be divided into external and internal factors. External factors
404 include temporal and spatial fluctuations in pressure, temperature, and As concentrations
405 within the pyrite-forming fluids (Chouinard et al., 2005; Shore and Fowler, 1996; Wu et
406 al., 2019a; Xing et al., 2019). In comparison, internal factors include the formation of
407 As-rich growth zones, patches, and oscillations as a result of crystal surface structure
408 effects (Chouinard et al., 2005; Dowty, 1976; Wu et al., 2019b), heteroepitaxial Stranski–
409 Krastanov (SK) growth (e.g., Kaiser, 2002; Mo et al., 1990; Wu et al., 2019b), and
410 diffusion-limited self-organization (e.g., Putnis et al., 1992; Wu et al., 2019b),
411 respectively. All of these previous research suggest that As is likely to be incorporated
412 into growing pyrite by fluid–pyrite interaction; in the fluid As exists most likely as the
413 neutral $As^{3+}(OH)_3(aq)$ complex, whereas Au exists as bisulfide complex ($Au^{+}HS(aq)$ or
414 $Au^{+}(HS)_2^{-}$; James-Smith et al. 2010; Liu et al. 2014; Pokrovski et al. 2014; Zhong et al.
415 2015). In particular, ICDR can be an important control on phase transformation during
416 fluid–rock interactions (e.g., Altree-Williams et al., 2015; Putnis, 2009). Sung et al. (2009)
417 suggested that the primary zoning of As within pyrite is disturbed by ICDR processes that
418 generate permeable porosity within regions undergoing replacement. It is likely that
419 ICDR formed some of the As-rich rims within the Qiucun pyrite due to the typical
420 textural features including (1) sharp and curvilinear interfaces (Figs. 3, 8–10) rather than
421 diffuse phase boundaries between As-rich and -deficient pyrite domains, (2) As-rich
422 zonal rims that preserve the morphology of the As-deficient pyrite interior (Fig. 3d, f),
423 (3) the epitaxial growth of As-rich zonal rims around early As-deficient cores (Figs. 6, 8,

10), and (4) fissures and pore spaces within the region undergoing reaction, facilitating fluid access to the reaction interface, and leading to increased replacement of the parent pyrite (Fig. 3d, f). However, some As-rich zones within this pyrite are free of significant porosity (Fig. 3b, e). These zones suggest that As-pyrite may have grown on the surfaces of pre-existing pyrite. It is also possible that these zones are controlled by ICDR, with solid-state diffusion processes causing the reduction of porosity (Zhao et al., 2014). This means that it is difficult to determine the role of hydrothermal alteration in the formation of As-rich pyrite zones, but the fact that variations in conditions (e.g., pressure, temperature, pH, and composition) at fluid–pyrite reaction interfaces are certainly key in controlling the incorporation of As into pyrite.

Incorporation of invisible gold within arsenian pyrite

Multiple forms of invisible Au occur in natural or synthetic pyrite samples, including solid solution (Au^{+}), nanoparticles (Au^{0}), and Au_2S-like clusters as outlined in the introduction. As such, one key variable is the form of invisible Au which predominates within As-pyrite. Wu et al. (2019b) utilized APT to show that Au atoms were bound with As atoms and hosted in solid solution (Au^{+}) within As-pyrite from the Daqiao Au deposit. Gopon et al. (2019) also used APT to report the absence of Au nanoclusters within As-pyrite from some Carlin-type Au deposits. Any Au nanoclusters (~50 nm; Palenik et al., 2004) present within pyrite should be detectable by a combination of APT and TEM analyses of the auriferous pyrite (as identified using MSXRF and LA–ICP–MS) analyzed during our study. In addition, the Au/As ratios of the samples analyzed during our study all plot beneath the solubility limit above which Au is present as nanoparticles (Reich et

447 al., 2005), explaining the absence of these nanoparticles from the pyrite in the study area.
448 The data presented in this study cannot preclude the presence of Au or Au_2S-like
449 nanoparticles, but it is probable that the invisible Au within the As-rich pyrite in the study
450 area was mainly incorporated by solid solution.

451 The solid solution incorporation of Au in pyrite is thought to occur as a result of the
452 substitution of monovalent Au for Fe^{2+} (e.g., Filimonova et al., 2020; Merkulova et al.,
453 2019; Trigub et al., 2017). However, this substitution is expected to be inhibited by the
454 size discrepancy between the Au–S bond (2.41 Å) and Fe–S bond (2.26 Å) within pyrite
455 (Filimonova et al., 2020), and by ion charge imbalance (e.g., Deditius et al., 2008;
456 Merkulova et al., 2019; Simon et al., 1999). Previous research has identified a close
457 association between Au and As within arsenian pyrite (e.g., Arehart et al., 1993; Deditius
458 et al., 2014; Fleet et al., 1993; Fleet and Mumin, 1997; Morishita et al., 2018; Reich et al.,
459 2005). This is thought to represent the geochemical signature for atomic scale Au–As
460 coordination (Merkulova et al., 2019). Gopon et al. (2019) identified areas of increased
461 concentration of As surrounding Au ions within an APT reconstruction, validating the
462 hypothesis (Fleet and Mumin, 1997) that Au ions could be incorporated into As-rich,
463 Fe-deficient pyrite growth surfaces where Au is hosted in vacancies in nearest neighbor
464 cation sites and is fixed by soft Lewis bases (e.g., As_2 and AsS). The marked positive
465 correlation between As and Au (Figs. 4–5) within the samples from the study area can be
466 explained by the processes outlined above. The coupled substitution of $As^{3+} + Au^{+} \Leftrightarrow$
467 $2Fe^{2+}$ (Deditius et al., 2008) is unlikely to have occurred as As^{-} occupies the S site in the
468 pyrite from the study area as outlined above.

469 Furthermore, decoupling of As and Au chemistry was also demonstrated within some

As-pyrites (Filimonova et al., 2020). Nonetheless, As–S substitution is expected to create a more favorable local environment for hosting Au in As-pyrite than pure pyrite, as arsenic can stabilize Au-bearing phases and result in a higher solubility of Au (Deditius et al., 2014; Reich et al., 2005; Trigub et al., 2017). Further evidence is from calculations by Blanchard et al. (2007) and Manceau et al. (2020) which predicted that the lowest energy bonding environment of As in pyrite is similar to local structure of As in arsenopyrite, with chemically bound Au reported to be thermodynamically more stable in arsenopyrite or löllingite than in pyrite (Filimonova et al., 2020; Trigub et al., 2017).

In principle, the more As is incorporated into pyrite by substitution for S, the higher the density of defects within the crystal structure (Fleet and Mumin, 1997; Gopon et al., 2019). Planar structures such as stacking faults and dislocations record a monotonic increase in As concentrations as evidenced by APT analysis (Dubosq et al., 2019). Other APT analysis indicates that impurities such as Pb and Sb also occur as 5–10 nm clusters within dislocations and high-angle grain boundaries (Fougerouse et al., 2019). The new data presented in this study indicate that stacking faults are present in As-pyrite (~ 8wt% As; Fig. 10), but absent in this sample (~ 4 wt% As; Fig. 7). These stacking faults reflect the presence of single (1 0 1) layers of marcasite that disrupt the regular sequence of (0 0 2) layers in pyrite (Dodony et al., 1996), which is related to the introduction of As into the pyrite structure (Reich and Becker, 2006; Simon et al., 1999). The presence of galena nanoparticles within these fine layers suggests that As-induced marcasite-type lamellae act as a preferential conduit for the migration and enrichment of trace elements (e.g., Au) within the pyrite lattice. The stacking faults within arsenian pyrite crystals also favor the incorporation of impurity elements as nanoparticles, leading to not only the

493 heterogeneous distribution of trace elements, but also changes in the mode of occurrence
494 of these elements.

495 Gold nanoparticles are thought to preferentially occur in polycrystalline As-rich
496 pyrite domains instead of highly crystalline domains within pyrite (Palenik et al., 2004).
497 Combining this previous research with the data presented in this study suggests that As
498 controls the mode of Au incorporation into pyrite in two different ways. The first of these
499 is the solubility limit defined by As contents (Reich et al., 2005) and the associated
500 As-induced expansion of pyrite unit-cells. This affects highly crystalline pyrite domains
501 and limits the presence of Au nanoparticles in these areas. In comparison, poorly
502 crystalline domains have As-induced faulted structures (e.g., stacking faults) that
503 preferentially host Au nanoparticles. This hypothesis can explain the presence of Au
504 nanoparticles below the solubility limit within the high-As pyrite (e.g., Fougerouse et al.,
505 2016b). This in turn means that the model of Reich et al. (2005) should be used with
506 caution when discriminating between the different modes for the incorporation of Au into
507 pyrite.

508

509 **Fluid evolution and gold scavenging processes**

510 The Qiucun deposit records two stages of hydrothermal fluid activity, which are
511 (1) early fluids that formed As- and Au-deficient pyrite and (2) late fluids that formed As-
512 and Au-rich pyrite. The formation of electrum is closely associated with the later stage
513 fluid as evidenced by (1) the presence of the majority of electrum inclusions at the
514 interface between As-rich and -deficient domains (Figs. 3 and 5), (2) the replacement of
515 early-formed pyrite by electrum along fractures in the former (Fig. 3), and (3) the

516 presence of electrum inclusions along grain boundaries within As-deficient pyrite
517 domains (Fig. 6), most likely reflecting Au enrichment by diffusion along grain
518 boundaries (e.g., Dubosq et al., 2019; Fougerouse et al., 2019). All of this indicates that
519 the Au mineralization within the Qiucun deposit was associated with late-stage
520 hydrothermal fluid activity.

521 Multiple factors influence the incorporation of As and Au into pyrite. Reich and
522 Becker (2006) used *first principle* calculations to suggest that decreasing temperature
523 favors the ongoing ordering of As within the pyrite structure. The invisible Au in pyrite
524 also presented a retrograde behavior which means that elevated temperature results in a
525 decrease of invisible Au concentration in pyrite (Filimonova et al., 2020; Pokrovski et al.,
526 2019; Trigub et al., 2017). Additionally, fluid boiling within epithermal systems results in
527 the escape of volatile components (e.g., H_2S and CO_2) from hydrothermal fluids, causing
528 a decrease in sulfur fugacity and an increase in pH, and favoring the development of As
529 ordering within the pyrite structure (Spycher and Reed, 1989; Reich et al., 2005). Fluid
530 boiling is also an effective way of scavenging metals (e.g., Au) from hydrothermal fluids
531 (Brown, 1986; Cooke, 2000; Simmons et al., 2005), as a result of changes in
532 physico-chemical conditions (e.g., pH, temperature, and sulfur fugacity; Heinrich et al.,
533 2007). Fluid boiling is thought to be the main control on Au mineralization within the
534 Qiucun Au deposit as evidenced by data from fluid inclusions and petrographic and
535 textural analysis (Ni et al., 2018). Combining the results of this previous research with the
536 data presented in this study suggests that interfaces where As significantly substituted for
537 S within pyrite may reflect a period of fluid boiling that causes an abrupt drop in either S
538 fugacity or temperature or an increase in pH. These abrupt physico-chemical changes also

539 cause the destabilization of metal complexes (e.g., Au hydrosulfide complexes) and the
540 formation of a layer supersaturated in Au that precipitates numerous electrum inclusions
541 along this interface. From the perspective of the interface itself, fluid–rock interfaces can
542 stabilize the formation of metastable products and can cause the scavenging of trace
543 elements from hydrothermal fluids (Altree-Williams et al., 2015; Li et al., 2015;
544 Ruiz-Agudo et al., 2014; Tooth et al., 2011; Wu et al., 2019a). This interface associated
545 with the low effective surface energy facilitates the nucleation and crystallization of Au
546 ionic species as secondary phases.
547

548 **IMPLICATIONS**

549 This study confirms that As can be used as a proxy for Au within the Qiucun Au
550 deposit as the concentrations of these two elements have a strong positive correlation and
551 a coupled distribution. The new MSXRF, LA–ICP–MS, APT, and TEM data indicate that
552 invisible Au is mostly present as a homogeneous solid solution rather than as
553 nanoparticles within the hosting arsenian pyrite. Arsenic-induced changes in the pyrite
554 structure are potentially significant for the interpretation of the coupled geochemical
555 behavior of Au and As, especially as Au ions with larger effective ionic radii than both Fe
556 and S take up more space within the pyrite structure. Further research is needed to
557 investigate the Au and As occupations within the pyrite structure and the relationship
558 between these elements and lattice defects in various geological settings, all of which will
559 improve our understanding of the incorporation of invisible Au within sulfide minerals
560 and provide new insights into the effective processing of refractory Au-bearing ores.

561 The samples from the study area contain visible electrum inclusions that are

562 concentrated either at the interface between As-rich and -deficient pyrite domains or in
563 fractures and along grain boundaries within As-deficient pyrite domains. This distribution
564 of visible electrum probably reflects the fluid boiling process that caused Au
565 supersaturation and the precipitation of Au from hydrothermal fluids onto the fluid–pyrite
566 interface as a result of changes in physico-chemical conditions (e.g., pH, temperature,
567 and/or pressure).

568 Here, we present a conceptual model that outlines the processes involved in the
569 scavenging of Au from hydrothermal fluids (Fig. 15). Initially intense fluid–pyrite
570 reactions proceeded on the surface of pre-existing pyrite crystals and along grain
571 boundaries that provided 'pathways' for the diffusion of fluids into the pyrite. An abrupt
572 change in physico-chemical conditions (e.g., temperature, pH, and/or sulfur fugacity)
573 caused the supersaturation of Au ionic species at these sites. This, combined with low
574 effective surface energy, caused the nucleation of Au ions and the crystallization of
575 secondary electrum. Continuing fluid–pyrite reaction and a decrease in Au
576 supersaturation caused the system to evolve to As-assisted incorporation of Au into pyrite.
577 This study not only demonstrates the genetic relationship between the formation of
578 visible and invisible Au from hydrothermal fluids, but also emphasizes the significance of
579 systematic compositional and textural observations in interpreting fluid–rock interactions
580 and understanding the processes involved in the incorporation of trace elements into other
581 minerals. This indicates that determining mineral paragenetic sequences solely based on
582 the distribution and mode of mineral occurrences should be approached cautiously in
583 future research into ore-forming processes.

584

ACKNOWLEDGEMENTS

This study was financially supported by two NSFC projects (Grants 41272055, 41672037, and 41830426), National Key R&D Program of China (Grant 2016YFC0600205), China Geological Survey project (Grant 12120115034601), and joint Ph.D. project funding from the China Scholarship Council (Grant 201806190162). We are grateful to Juan Li for assistance during SEM imaging, Lixin Gu for assistance with FIB-SEM analysis, Wenlan Zhang and Wendi Chen for assistance with EMPA, Jianfeng Gao for assistance with LA–ICP–MS analysis, Baohong Zhang for EBSD analysis, Ashley Slattery, Zhidong Xie, Jiani Chen, and Xu Tang for TEM analysis, and Zhen He and Xiaoke Zhang for XRD analysis. Part of this research was undertaken at the XFM beamline at the Australian Synchrotron, Melbourne, Victoria, Australia, part of ANSTO. The authors also acknowledge Maarten Broekmans, Artur Deditius and three anonymous reviewers for their constructive comments on an earlier version of the manuscript.

REFERENCES CITED

Altree-Williams, A., Pring, A., Ngothai, Y., and Brugger, J. (2015) Textural and compositional complexities resulting from coupled dissolution–reprecipitation reactions in geomaterials. Earth-Science Reviews, 150, 628–651.

Arehart, G. B., Chryssoulis, S. L., and Kesler, S. E. (1993) Gold and arsenic in iron sulfides from sediment-hosted disseminated gold deposits; implications for depositional processes. Economic Geology, 88, 171–185.

Aylmore, M. G. (1995) Distribution and agglomeration of gold in arsenopyrite and pyrite. Curtin University.

608 Bakken, B. M., Hochella, M. F., Marshall, A. F., and Turner, A. M. (1989)
609 High-resolution microscopy of gold in unoxidized ore from the Carlin mine, Nevada.
610 Economic Geology, 84, 171–179.
611 Blanchard, M., Alfredsson, M., Brodholt, J., Wright, K., and Catlow, C. R. A. (2007)
612 Arsenic incorporation into FeS_2 pyrite and its influence on dissolution: a DFT study.
613 Geochimica et Cosmochimica Acta, 71, 624–630.
614 Brown, K. L. (1986) Gold deposition from geothermal discharges in New Zealand.
615 Economic Geology, 81, 979–983.
616 Chouinard, A., Paquette, J., and Williams-Jones, A. E. (2005) Crystallographic controls
617 on trace-element incorporation in auriferous pyrite from the Pascua epithermal
618 high-sulfidation deposit, Chile–Argentina. The Canadian Mineralogist, 43, 951–963.
619 Cook, N. J. and Chryssoulis, S. L. (1990) Concentrations of invisible gold in the common
620 sulfides. The Canadian Mineralogist, 28, 1–16.
621 Cooke, D. R. (2000) Characteristics and genesis of epithermal gold deposits. Reviews in
622 Economic Geology, 13, 221–244.
623 Deditius, A. P., Reich, M., Kesler, S. E., Utsunomiya, S., Chryssoulis, S. L., Walshe, J.,
624 and Ewing, R. C. (2014) The coupled geochemistry of Au and As in pyrite from
625 hydrothermal ore deposits. Geochimica et Cosmochimica Acta, 140, 644–670.
626 Deditius, A. P., Utsunomiya, S., Ewing, R. C., and Kesler S. E. (2009) Nanoscale “liquid”
627 inclusions of As–Fe–S in arsenian pyrite. American Mineralogist, 94, 391–394.
628 Deditius, A. P., Utsunomiya, S., Renock, D., Ewing, R. C., Ramana, C. V., Becker, U.,
629 and Kesler, S. E. (2008) A proposed new type of arsenian pyrite: Composition,
630 nanostructure and geological significance. Geochimica et Cosmochimica Acta, 72,

631 2919–2933.

632 del Real, I., Smieska, L., Thompson, J. F. H., Martinez, C., Thomas, J., and
633 Layton-Matthews, D. (2019) Using multiple micro-analytical techniques for
634 evaluating quantitative synchrotron-XRF elemental mapping of hydrothermal pyrite.
635 Journal of Analytical Atomic Spectrometry, 34, 1724–1738.

636 Dodony, I., Posfal, M., and Buseck, P. R. (1996) Structural relationship between pyrite
637 and marcasite. American Mineralogist, 81, 119–125.

638 Dowty, E. (1976) Crystal structure and crystal growth: II. Sector zoning in minerals.
639 American Mineralogist, 61, 460–469.

640 Dubosq, R., Rogowitz, A., Schweinar, K., Gault, B., and Schneider, D. A. (2019) A 2D
641 and 3D nanostructural study of naturally deformed pyrite: assessing the links
642 between trace element mobility and defect structures. Contributions to Mineralogy
643 and Petrology, 174, 72.

644 Etschmann, B. E., Ryan, C. G., Brugger, J., Kirkham, R., Hough, R. M., Moorhead, G.,
645 Siddons, D. P., De Geronimo, G., Kuczewski, A., Dunn, P., Paterson, D., de Jonge, M.
646 D., Howard, D. L., Davey, P., and Jensen, M. (2010) Reduced As components in
647 highly oxidized environments: Evidence from full spectral XANES imaging using
648 the Maia massively parallel detector. American Mineralogist, 95, 884–887.

649 FIGSR: Fujian Institute of Geological Survey and Research, 2014. Regional geology and
650 mineral resources map in the central-east of Fujian Province. Geol. Map.

651 Filimonova, O. N., Tagirov, B. R., Trigub, A. L., Nickolsky, M. S., Rovezzi, M., Belogub,
652 E. V., Reukov, V .L., and Vikentyev, I. V. (2020) The state of Au and As in pyrite
653 studied by X-ray absorption spectroscopy of natural minerals and synthetic phases.

654 Ore Geology Reviews, 121, 103475.

655 Fisher, L., Fougerouse, D., Cleverley, J., Ryan, C., Micklethwaite, S., Halfpenny, A.,
656 Hough, R., Gee, M., Paterson, D., and Howard, D. (2014) Quantified, multi-scale
657 X-ray fluorescence element mapping using the Maia detector array: Application to
658 mineral deposit studies. Mineralium Deposita, 50, 665–674.

659 Fleet, M. E., Chryssoulis, S. L., MacLean, P. J., Davidson, R., and Weisener, C. G. (1993)
660 Arsenian pyrite from gold deposits; Au and As distribution investigated by SIMS and
661 EMP, and color staining and surface oxidation by XPS and LIMS. The Canadian
662 Mineralogist, 31, 1–17.

663 Fleet, M. E. and Mumin, A. H. (1997) Gold-bearing arsenian pyrite and marcasite and
664 arsenopyrite from Carlin Trend gold deposits and laboratory synthesis. American
665 Mineralogist, 82, 182–193.

666 Fougerouse, D., Micklethwaite, S., Tomkins, A. G., Mei, Y., Kilburn, M., Guagliardo, P.,
667 Fisher, L. A., Halfpenny, A., Gee, M., and Paterson, D. (2016a) Gold remobilisation
668 and formation of high grade ore shoots driven by dissolution-reprecipitation
669 replacement and Ni substitution into auriferous arsenopyrite. Geochimica et
670 Cosmochimica Acta, 178, 143–159.

671 Fougerouse, D., Reddy, S. M., Kirkland, C. L., Saxey, D. W., Rickard, W. D., and Hough,
672 R. M. (2019) Time-resolved, defect-hosted, trace element mobility in deformed
673 Witwatersrand pyrite. Geoscience Frontiers, 10, 55–63.

674 Fougerouse, D., Reddy, S. M., Saxey, D. W., Rickard, W. D., Van Riessen, A., and
675 Micklethwaite, S. (2016b) Nanoscale gold clusters in arsenopyrite controlled by
676 growth rate not concentration: Evidence from atom probe microscopy. American

677 Mineralogist, 101, 1916–1919.
678 Gao, J. F., Jackson, S. E., Dubé, B., Kontak, D. J., De Souza, S., Dubé, B., and
679 Mercier-Langevin, P. (2015) Genesis of the Canadian Malartic, Côté Gold, and
680 Musselwhite gold deposits: Insights from LA-ICP-MS element mapping of pyrite.
681 Targeted geoscience initiative, 4, 157–175.
682 Geisler, T., Schaltegger, U., and Tomaschek, F. (2007) Re-equilibration of zircon in
683 aqueous fluids and melts. Elements, 3, 43–50.
684 Gopon, P., Douglas, J. O., Auger, M. A., Hansen, L., Wade, J., Cline, J. S., Robb, L. J.,
685 and Moody, M. P. (2019) A Nanoscale Investigation of Carlin-Type Gold Deposits:
686 An Atom-Scale Elemental and Isotopic Perspective. Economic Geology, 114, 1123–
687 1133.
688 Guilin Geology and Mining Limited Company, 2003. Internal report.
689 Harlov, D. E., Wirth, R., and Hetherington, C. J. (2011) Fluid-mediated partial alteration
690 in monazite: the role of coupled dissolution–reprecipitation in element redistribution
691 and mass transfer. Contributions to Mineralogy and Petrology, 162, 329–348.
692 Heinrich, C. A. (2007) Fluid-fluid interactions in magmatic-hydrothermal ore formation.
693 Reviews in Mineralogy and Geochemistry, 65, 363–387.
694 Holland, T.J.B. and Redfern, S.A.T. (1997) Unit cell refinement from powder diffraction
695 data: the use of regression diagnostics. Mineralogical Magazine, 61, 65–77.
696 Huang, B., Ni, P., Xiang, H. L., Wang, G. G., Yang, Y. L., Pan, J. Y., Li, S. N., and Bao. T.
697 (2017) The geological characteristics and ore genesis of the Qiucun gold deposit,
698 Fujian Province. Bulletin of Mineralogy, Petrology and Geochemistry, 36, 650–659.
699 Hunter, B. A. (1998) Rietica A Visual Rietveld Program in: Commission on Powder

Diffraction Newsletter, 20, 1998.

James-Smith, J., Cauzid, J., Testemale, D., Liu, W., Hazemann, J.-L., Proux, O., Etschmann, B., Philippot, P., Banks, D., Williams, P. and Brugger, J. (2010) Arsenic speciation in fluid inclusions using X-ray Absorption Spectroscopy. American Mineralogist, 95, 921–932

Kaiser, N. (2002) Review of the fundamentals of thin-film growth. Applied Optics, 41, 3053–3060.

La Fontaine, A., Piazolo, S., Trimby, P., Yang, L. M., and Cairney, J. M. (2017) Laser-assisted atom probe tomography of deformed minerals: a zircon case study. Microscopy and Microanalysis, 23, 404–413.

Li, K., Brugger, J., and Pring, A. (2018a) Exsolution of chalcopyrite from bornite-digenite solid solution: An example of a fluid-driven back-replacement reaction. Mineralium Deposita, 53, 903–908.

Li, K., Etschmann, B., Rae, N., Reith, F., Ryan, C. G., Kirkham, R., Howard, D., Rosa, D. R. N., Zammit, C., Pring, A., Ngothai, Y., Hooker, A. and Brugger, J. (2016) Ore Petrography Using Megapixel X-Ray Imaging: Rapid Insights into Element Distribution and Mobilization in Complex Pt and U-Ge-Cu Ores. Economic Geology, 111, 487–501.

Li, K., Pring, A., Etschmann, B., Macmillan, E., Ngothai, Y., O'Neill, B., Hooker, A., Mosselmans, F., and Brugger, J. (2015) Uranium scavenging during mineral replacement reactions. American Mineralogist, 100, 1728–1735.

Li, S. N., Ni, P., Bao, T., Li, C. Z., Xiang, H. L., Wang, G. G., Huang, B., Chi, Z., Dai, B. Z., and Ding, J. Y. (2018b) Geology, fluid inclusion, and stable isotope systematics of

723 the Dongyang epithermal gold deposit, Fujian Province, southeast China:
724 Implications for ore genesis and mineral exploration. Journal of Geochemical
725 Exploration, 195, 16–30.
726 Li, Y., Chen, J., Chen, Y., Zhao, C., Lee, M. H., and Lin, T. H. (2018c) DFT+ U study on
727 the electronic structures and optical properties of pyrite and marcasite.
728 Computational Materials Science, 150, 346–352.
729 Liang, J. L., Sun, W. D., Li, Y. L., Zhu, S. Y., Li, H., Liu, Y. L., and Zhai, W. (2013) An
730 XPS study on the valence states of arsenic in arsenian pyrite: implications for Au
731 deposition mechanism of the Yang-shan Carlin-type gold deposit, western Qinling
732 belt. Journal of Asian Earth Sciences, 62, 363–372.
733 Liu, Y., Hu, Z., Gao, S., Günther, D., Xu, J., Gao, C., and Chen, H. (2008) In situ analysis
734 of major and trace elements of anhydrous minerals by LA-ICP-MS without applying
735 an internal standard. Chemical Geology, 257, 34–43.
736 Liu, W., Etschmann, B., Testemale, D., Hazemann, J.-L., Rempel, K., Müller, H. and
737 Brugger, J., 2014. Gold transport in hydrothermal fluids: competition among the Cl^-,
738 Br^-, HS^- and NH_3(aq) ligands. Chemical Geology, 376, 11–19.
739 Manceau, A., Merkulova, M., Mathon, O., Glatzel, P., Murdzek, M., Batanova, V.,
740 Simionovici, A., Steinmann, S.N., and Paktunc, D. (2020) The mode of incorporation
741 of As (-I) and Se (-I) in natural pyrite revisited. ACS Earth and Space Chemistry, 4,
742 379–390.
743 Merkulova, M., Mathon, O., Glatzel, P., Rovezzi, M., Batanova, V., Philippe, M., Boiron,
744 M. C., and Manceau, A. (2019) Revealing the Chemical Form of “Invisible” Gold in
745 Natural Arsenian Pyrite and Arsenopyrite with High Energy-Resolution X-ray

Absorption Spectroscopy. ACS Earth and Space Chemistry, 3, 1905–1914.

Mo, Y. W., Savage, D. E., Swartzentruber, B. S., and Lagally, M. G. (1990) Kinetic pathway in Stranski-Krastanov growth of Ge on Si (001). Physical Review Letters, 65, 1020–1023.

Morishita, Y., Shimada, N., and Shimada, K. (2018) Invisible gold in arsenian pyrite from the high-grade Hishikari gold deposit, Japan: Significance of variation and distribution of Au/As ratios in pyrite. Ore Geology Reviews, 95, 79–93.

Ni, P., Pan, J. Y., Huang, B., Wang, G. G., Xiang, H. L., Yang, Y. L., Li, S. N., and Bao, T. (2018) Geology, ore-forming fluid and genesis of the Qiucun gold deposit: Implication for mineral exploration at Dehua prospecting region, SE China. Journal of Geochemical Exploration, 195, 3–15.

Palenik, C. S., Utsunomiya, S., Reich, M., Kesler, S. E., Wang, L. M., and Ewing, R. C. (2004) "Invisible" gold revealed: Direct imaging of gold nanoparticles in a Carlin-type deposit. American Mineralogist, 89, 1359–1366.

Pals, D. W., Spry, P. G., and Chryssoulis, S. (2003) Invisible gold and tellurium in arsenic-rich pyrite from the Emperor gold deposit, Fiji: implications for gold distribution and deposition. Economic Geology, 98, 479–493.

Pokrovski, G. S., Kokh, M. A., Proux, O., Hazemann, J. L., Bazarkina, E. F., Testemale, D., Escoda, C., Boiron, M. C., Blanchard, M., Aigouy, T., Gouy, S., de Parseval, P., and Thibaut, M. (2019) The nature and partitioning of invisible gold in the pyrite–fluid system. Ore Geology Reviews, 109, 545–563.

Pokrovski, G.S., Akinfiev, N.N., Borisova, A.Y., Zotov, A.V. and Kouzmanov, K. (2014) Gold speciation and transport in geological fluids: insights from experiments and

769 physical-chemical modeling. In: Garofalo, P., Ripley, E. (Eds.), Gold-Transporting
770 Fluids in the Earth's Crust. In: Geological Society of London Special Publications
771 402, 9–70.
772 Putnis, A. (2009) Mineral replacement reactions. Reviews in Mineralogy and
773 Geochemistry, 70, 87–124.
774 Putnis, A., Fernandez-Diaz, L., and Prieto, M. (1992) Experimentally produced
775 oscillatory zoning in the (Ba, Sr)SO_4 solid solution. Nature, 358, 743–745.
776 Qian, G. J., Brugger, J., Testemale, D., Skinner, W., and Pring, A. (2013) Formation of
777 As(II)-pyrite during experimental replacement of magnetite under hydrothermal
778 conditions. Geochimica et Cosmochimica Acta, 100, 1–10.
779 Reich, M. and Becker, U. (2006) First-principles calculations of the thermodynamic
780 mixing properties of arsenic incorporation into pyrite and marcasite. Chemical
781 Geology, 225, 278–290.
782 Reich, M., Kesler, S. E., Utsunomiya, S., Palenik, C. S., Chryssoulis, S. L., and Ewing, R.
783 C. (2005) Solubility of gold in arsenian pyrite. Geochimica et Cosmochimica Acta,
784 69, 2781–2796.
785 Reich, M., Utsunomiya, S., Kesler, S. E., Wang, L., Ewing, R. C., and Becker, U. (2006)
786 Thermal behavior of metal nanoparticles in geologic materials. Geology, 34, 1033–
787 1036.
788 Rietveld, H. (1969) A profile refinement method for nuclear and magnetic structures.
789 Journal of applied Crystallography, 2, 65–71.
790 Ruiz-Agudo, E., Putnis, C. V., and Putnis, A. (2014) Coupled dissolution and
791 precipitation at mineral–fluid interfaces. Chemical Geology, 383, 132–146.

792 Savage, K.S., Tingle, T.N., O'Day, P.A., Waychunas, G.A., and Bird, D.K. (2000) Arsenic
793 speciation in pyrite and secondary weathering phases, Mother Lode gold district,
794 Tuolumne County, California. Applied Geochemistry, 15, 1219–1244.
795 Shore, M. and Fowler, A. D. (1996) Oscillatory zoning in minerals: A common
796 phenomenon. Canadian Mineralogist, 34, 1111–1126.
797 Simon, G., Huang, H., Penner-Hahn, J. E., Kesler, S. E., and Kao, L. S. (1999) Oxidation
798 state of gold and arsenic in gold-bearing arsenian pyrite. American mineralogist, 84,
799 1071–1079.
800 Simmons, S. F., White, N. C., and John, D. A. (2005) Geological characteristics of
801 epithermal precious and base metal deposits. Economic Geology 100th Anniversary,
802 29, 485–522.
803 Spycher N. F. and Reed M. H. (1989) As(III) and Sb(III) sulfide complexes; an evaluation
804 of stoichiometry and stability from existing experimental data. Geochimica et
805 Cosmochimica Acta, 53, 2185–2194.
806 Sung, Y. H., Brugger, J., Ciobanu, C. L., Pring, A., Skinner, W., and Nugus, M. (2009)
807 Invisible gold in arsenian pyrite and arsenopyrite from a multistage Archaean gold
808 deposit: Sunrise Dam, Eastern Goldfields Province,Western Australia. Mineralium
809 Deposita, 44, 765–791.
810 Sutton, S.R., Bertsch, P. M., Newville, M., Rivers, M., Lanzirotti, A., and Eng, P. (2002)
811 Microfluorescence and microtomography analyses of heterogeneous earth and
812 environmental materials. Reviews in Mineralogy and Geochemistry, 49, 429–483.
813 Tooth, B., Ciobanu, C.L., Green, L., O'Neill, B., and Brugger, J. (2011) Bi-melt
814 formation and gold scavenging from hydrothermal fluids: An experimental study.

Geochimica et Cosmochimica Acta, 75, 5423–5443.

Trigub, A. L., Tagirov, B. R., Kvashnina, K. O., Chareev, D. A., Nickolsky, M. S., Shiryaev, A. A., Baranova, N. N., Kovalchuk, E. V., and Mokhov, A. V. (2017) X-ray spectroscopy study of the chemical state of “invisible” Au in synthetic minerals in the Fe–As–S system. American Mineralogist, 102, 1057–1065.

Wu, R., Zheng, Y. F., Zhang, X. G., Sun, Y. F., Xu, J. B., and Jian, J. K. (2004) Hydrothermal synthesis and crystal structure of pyrite. Journal of Crystal Growth, 266, 523–527.

Wu, Y. F., Evans, K., Li, J. W., Fougerouse, D., Large, R. R., and Guagliardo, P. (2019a) Metal remobilization and ore-fluid perturbation during episodic replacement of auriferous pyrite from an epizonal orogenic gold deposit. Geochimica et Cosmochimica Acta, 245, 98–117.

Wu, Y. F., Fougerouse, D., Evans, K., Reddy, S. M., Saxey, D. W., Guagliardo, P., amd Li, J. W. (2019b) Gold, arsenic, and copper zoning in pyrite: a record of fluid chemistry and growth kinetics. Geology, 47, 641–644.

Xia, F., Brugger, J., Chen, G., Ngothai, Y., O'Neill, B., Putnis, A., and Pring, A. (2009) Mechanism and kinetics of pseudomorphic mineral replacement reactions: A case study of the replacement of pentlandite by violarite. Geochimica et Cosmochimica Acta, 73, 1945–1969.

Xing, Y., Brugger, J., Tomkins, A., and Shvarov, Y. (2019) Arsenic evolution as a tool for understanding formation of pyritic gold ores. Geology, 47, 335–338.

Xu, N., Li, S. R., Santosh, M., and Tong, B. (2018) Petrology, geochemistry and zircon U-Pb geochronology of the Jurassic porphyry dykes in the Dehua gold field,

838 Southeast China: Genesis and geodynamics. Geological Journal, 53, 547–564.
839 Xu, N., Li, S. R., Wu, C. L., and Santosh, M. (2019) Geochemistry and geochronology of
840 the Dongyang gold deposit in southeast China: Constraints on ore genesis.
841 Geological Journal, 1–14.
842 Zachariáš, J., Frýda, J., Paterová, B., and Mihaljevič, M. (2004) Arsenopyrite and
843 As-bearing pyrite from the Roudný deposit, Bohemian Massif. Mineralogical
844 Magazine, 68, 31–46.
845 Zhang, H., Cai, Y. F., Ni, P., and Zhang, Y. (2017) The occurrence mechanism of gold in
846 pyrite from the Qiucun gold deposit in Fujian Province, China. Acta Geologica
847 Sinica (English Edition), 91, 61–62.
848 Zhang, H., Cai, Y. F., Zhang, Y., Ni, P., Li, S. N., Ding, J. Y., Pan, Y. G., and Bao, T.
849 (2018) Mineralogical characteristics of silver minerals from the Dongyang Gold
850 deposit, China: Implications for the evolution of epithermal metallogenesis. Journal
851 of Geochemical Exploration, 195, 143–156.
852 Zhao, J., Brugger, J., Grguric, B. A., Ngothai, Y., and Pring, A. (2017) Fluid-enhanced
853 coarsening of mineral microstructures in hydrothermally synthesized bornite–
854 digenite solid solution. ACS Earth and Space Chemistry, 1, 465–474.
855 Zhao, J., Brugger, J., Grundler, P. V., Xia, F., Chen, G., and Pring, A. (2009) Mechanism
856 and kinetics of a mineral transformation under hydrothermal conditions: Calaverite
857 to metallic gold. American Mineralogist, 94, 1541–1555.
858 Zhao, J., Brugger, J., Ngothai, Y., and Pring, A. (2014). The replacement of chalcopyrite
859 by bornite under hydrothermal conditions. American Mineralogist, 99, 2389–2397.
860 Zhao, J., Brugger, J., Xia, F., Ngothai, Y., Chen, G., and Pring, A. (2013)

Dissolution-reprecipitation vs. solid-state diffusion: Mechanism of mineral transformations in sylvanite, $(AuAg)_2Te_4$, under hydrothermal conditions. American Mineralogist, 98, 19–32.

Zhong, R., Brugger, J., Chen, Y., Tomkins, A. and Li, W., 2015. Fate of gold and base metals during metamorphic devolatilization of a pelite. Geochimica et Cosmochimica Acta, 171, 338–352.

This is the peer-reviewed, final accepted version for American Mineralogist, published by the Mineralogical Society of America.
The published version is subject to change. Cite as Authors (Year) Title. American Mineralogist, in press.
DOI: https://doi.org/10.2138/am-2021-7675. http://www.minsocam.org/

868 **Figure Captions**

869 **Fig. 1.** (a) Map showing the location of Fujian Province in China. (b) Map showing the
870 major geological units, regional structures, and distribution of Au deposits within Fujian
871 Province, China (after Li et al., 2018b).

872 **Fig. 2.** (a–b) Photographs and (c–f) photomicrographs of polished thin-sections taken
873 under reflected light showing representative examples of mineralization within the
874 Qiucun deposit. (a) Pyrite-rich vein containing colloform-banded quartz. (b)
875 Pyrite-bearing quartz–chalcedony vein (modified after Ni et al., 2018). (c) Electrum and
876 chalcopyrite inclusions within pyrite crystals or present as fracture-filling veins. The
877 pyrite also contains minor amounts of sphalerite. The locations of LA–ICP–MS analyses
878 are indicated, along with measured Au concentrations (in ppm; Appendix Table S1). (d)
879 Electrum and sphalerite inclusions within pyrite. (e) Electrum and Ag sulfosalt
880 association present as inclusions within pyrite. (f) Pyrite with growth zoning from an
881 inclusion-rich core to a relatively clean rim. The dashed line indicates the boundary
882 between pyrite core and rim. Abbreviations: Ilt = illite, Py = pyrite, Qtz = quartz, Chc =
883 chalcedony, Ccp = chalcopyrite, Sp = sphalerite, Elc = electrum, and J_3n = Jurassic
884 Nanyuan Formation.

885 **Fig. 3.** BSE images showing the distribution of As and metal-bearing grains within pyrite
886 from the Qiucun deposit. (a–c) As-rich patches within pyrite showing that the majority of
887 electrum grains are located at the interface between As-rich and -deficient pyrite domains
888 (a–b), present as inclusions in the As-deficient pyrite interior (a, c), or present as
889 fracture-filling veins (a, c). The inset in (c) shows the distribution of
890 sub-micrometer-scale electrum. (d–f) As-rich zoned rims surrounding As-deficient pyrite

cores. The inset in (d) suggests that sphalerite and hessite are associated. The majority of the electrum is located at the interface between As-rich and -deficient domains (e–f), with some electrum present as fracture-filling veins (f). Local interfaces between As-rich and -deficient pyrite domains are highlighted by white dashed lines. EMPA locations and associated As concentrations are shown as orange circles and associated values (in wt%), with the locations of the three areas used for APT analysis (S1–S3) shown as orange rectangles. Abbreviations are as in Fig. 2 with b.l. = below detection limit and Hes = hessite.

Fig. 4. Diagram showing variations in the concentrations of Au and As within pyrite from the Qiucun deposit. The inferred solubility limit for Au is approximated by the line $C_{Au} = 0.02C_{As} + (4 \times 10^{-5})$, where C_{Au} and C_{As} represent the concentrations of Au and As, respectively (modified after Reich et al., 2005).

Fig. 5. K–Au–As RGB (red = K; green = Au; blue = As) image derived from the MSXRF mapping of an Au ore sample from the Qiucun deposit. The location of the three Au MSXRF images (a-c) and the BSE image (c–2) are shown as white rectangles in the main K–Au–As MSXRF image. (d) Close-up image of the region shown in the main RGB image. Abbreviations are as in Fig. 2.

Fig. 6. Results of the EBSD analysis of selected arsenian pyrite from the Qiucun Au deposit. (a) BSE image showing the analyzed pyrite grains. (b) Colored EBSD image showing the crystallographic misorientation within selected pyrite grains. The majority of crystallographic misorientations are > 5° other than those highlighted by the green dashed lines, which indicate misorientations of > 2°. The regions chosen for LA–ICP–MS analysis are shown as white crosses. Abbreviations are as in Fig. 2 with FIB-cut =

914 focused ion beam cut.

915 **Fig. 7.** (a) BSE image showing the location of FIB-cut analysis in As-pyrite from the
916 Qiucun deposit. (b–c) HAADF images showing the location of Ag–Sb and chalcopyrite
917 nanoparticles within As-pyrite, as well as associated SAED patterns (d–e). The EDS
918 spectra of the As-Sb nanoparticles are shown in appendix Fig. S5. (f) Image showing the
919 presence of polycrystalline domains within As-pyrite. (g–h) Fast-Fourier transform
920 images for the regions highlighted with dash lines in (f). Abbreviations are as in Fig. 2
921 with NP = nanoparticle.

922 **Fig. 8.** (a) Plan view of the location of the FIB-cut within an arsenian pyrite from the
923 Qiucun deposit. (b–c) SAED patterns for As-deficient and -rich pyrite domains of the
924 arsenian pyrite shown in (a), respectively. Abbreviations are as in Fig. 2.

925 **Fig. 9.** (a) Plan view of the location of the FIB-cut within an arsenian pyrite from the
926 Dongyang deposit. (b) HAADF image showing the As distribution within the FIB-cut. (c)
927 Close-up of the region highlighted with a rectangle in (b). (d–f) EDS STEM maps.
928 Abbreviations are as in Fig. 2 with Gn = galena.

929 **Fig. 10.** (a–c) HAADF–STEM images showing the distribution of stacking faults and
930 nanoparticles at this interface (Fig. 9). The insets show the atomic arrangements of the
931 Pb–Sb–S phases, with their EDS spectra shown in appendix Fig. S5. (d) Atomic
932 arrangements at the interface. (e) Close-up of the region highlighted with a rectangle in (d)
933 with a planar fault marked using an arrow. The inset shows the fast Fourier
934 transformation (FFT) image for As-pyrite. The d-spacings of the (2 0 0) plane are shown
935 as associated values. (f–g) Atomic arrangements in As-deficient and -rich pyrite domains,
936 respectively, with the associated d-spacings and FFT image.

937 **Fig. 11.** Results of the APT analysis of S1 showing maps of As, Ge, Sb, Cu, Pb, and Se
938 concentration where each sphere represents one atom. Scale bar is 40 nm.
939 **Fig. 12.** (a) Image showing the analysis location within the reconstructed volume of the
940 APT dataset. (b) 0.2 at% isosurface of combined Cu, Se and Pb atoms in the region
941 shown in (a). (c) Proximity histogram profile across the isosurface.
942 **Fig. 13.** (a) Image showing the analysis location within the reconstructed volume of the
943 APT dataset. (b) Nearest neighbor distribution analysis of the abundance of As, Sb, Pb,
944 Se, Ge, and Cu atoms for the region shown in (a).
945 **Fig. 14.** Results of the EMPA of arsenian pyrite from the Qiucun deposit. (a) Ternary Fe–
946 S–As (in at%) diagram comparing the composition of arsenian pyrite from the Qiucun Au
947 deposit (black circles) with data from Deditius et al. (2008; gray triangles). The former
948 indicates substitution of As for S (arrow 1), whereas the latter indicates substitution of As
949 for Fe (arrow 2). (b) Diagram showing variations in the concentrations of As and S within
950 arsenian pyrite.
951 **Fig. 15.** Schematic diagram showing the behavior of Au during the reaction between
952 pyrite and As–Au-rich fluids within the Qiucun Au deposit. Light gray areas indicate
953 early-formed As-deficient pyrite, dark gray areas indicate As-rich phases produced during
954 the reaction, black lines indicate grain boundaries, orange ellipsoids indicate visible
955 electrum inclusions, and orange crosses indicate Au ions. See text for detailed
956 explanation.
957

958 **Figures**

959 Figure 1

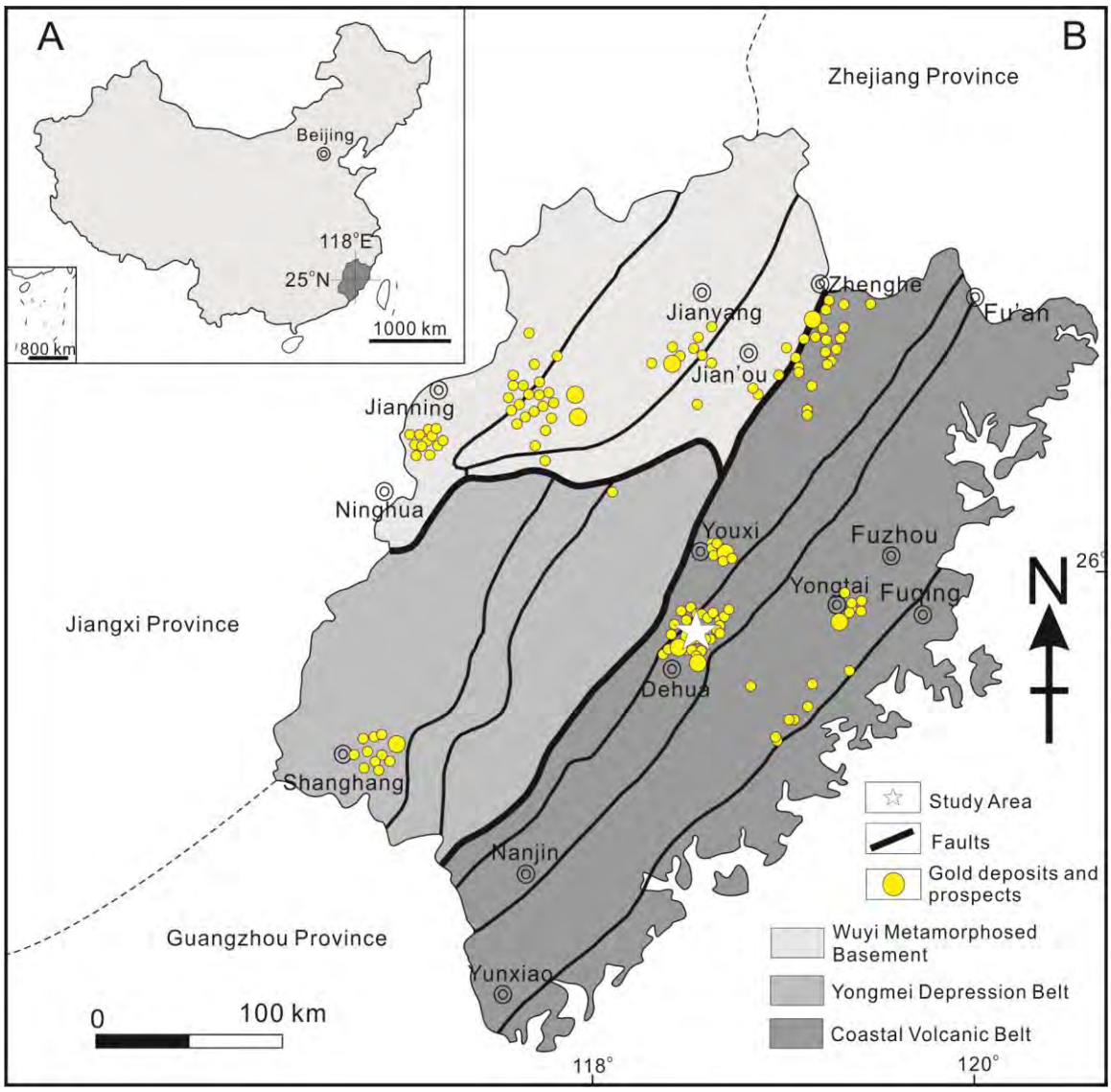

960

961

This is the peer-reviewed, final accepted version for American Mineralogist, published by the Mineralogical Society of America.
The published version is subject to change. Cite as Authors (Year) Title. American Mineralogist, in press.
DOI: https://doi.org/10.2138/am-2021-7675. http://www.minsocam.org/

962 Figure 2

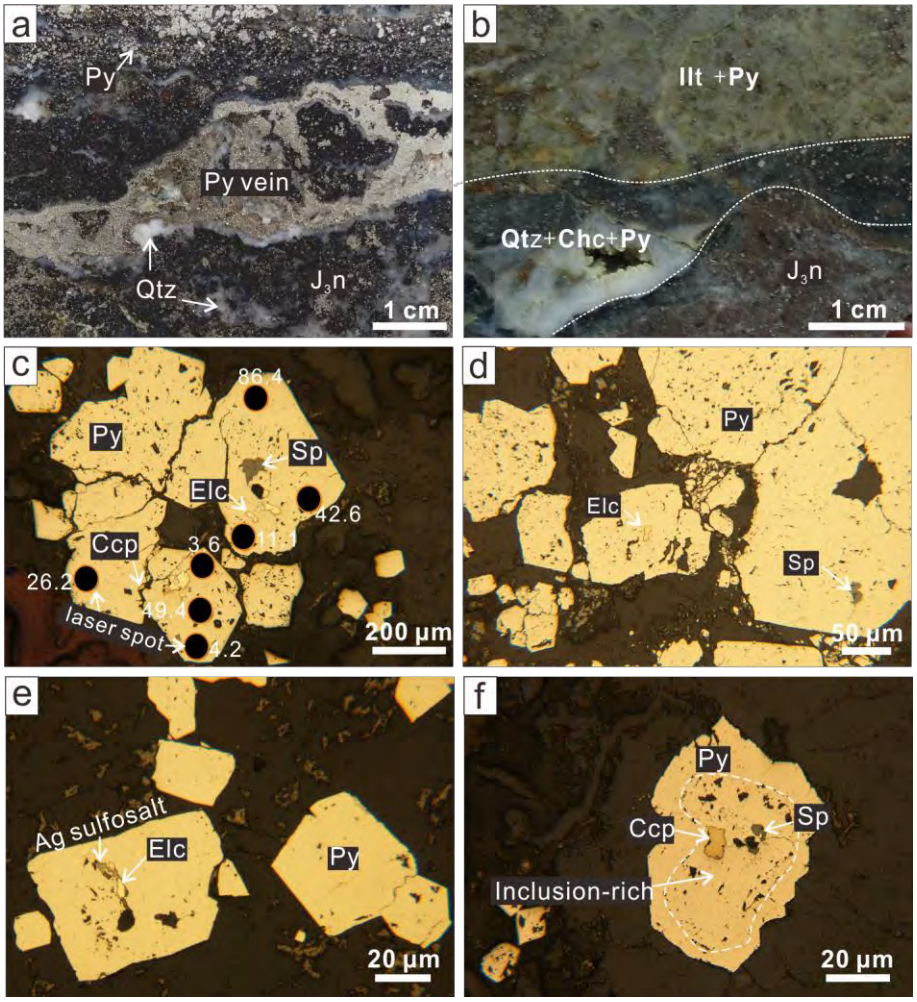

963

964

This is the peer-reviewed, final accepted version for American Mineralogist, published by the Mineralogical Society of America.
The published version is subject to change. Cite as Authors (Year) Title. American Mineralogist, in press.
DOI: https://doi.org/10.2138/am-2021-7675. http://www.minsocam.org/

965 Figure 3

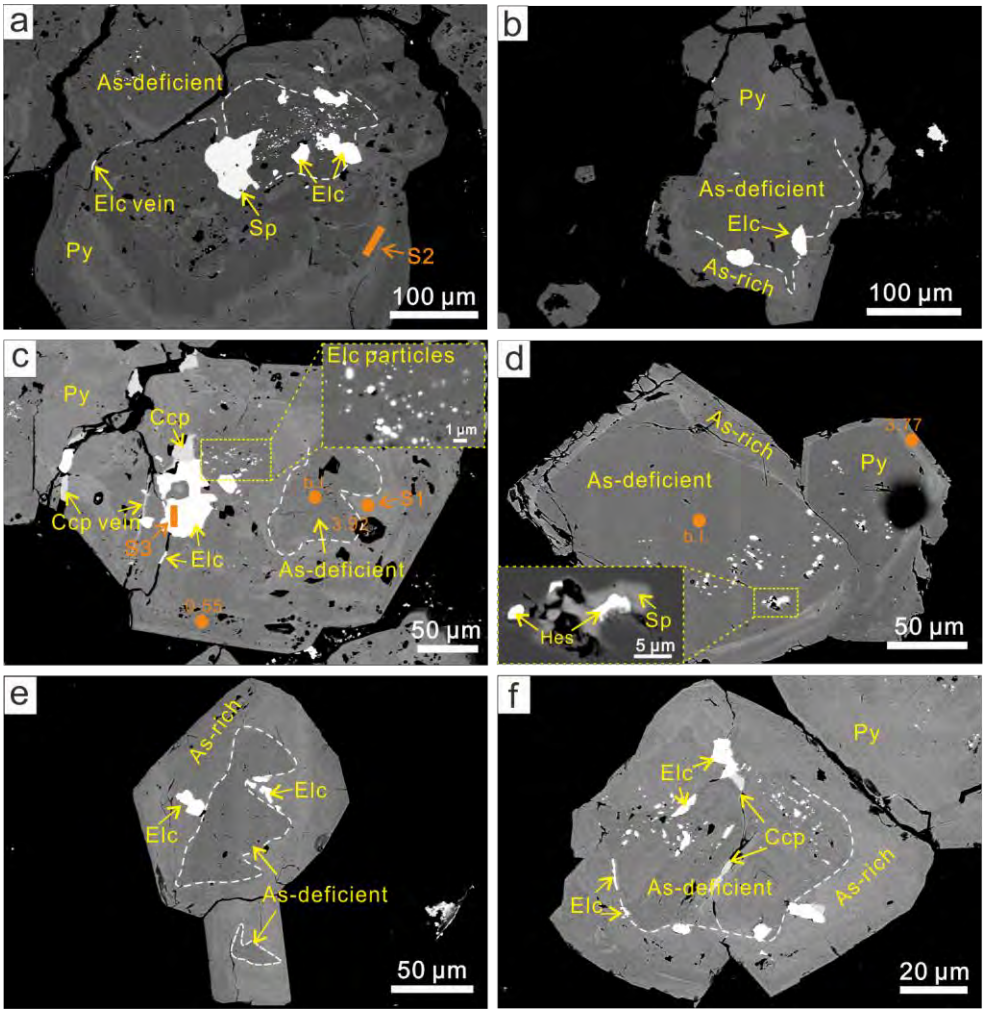

966

967 Figure 4

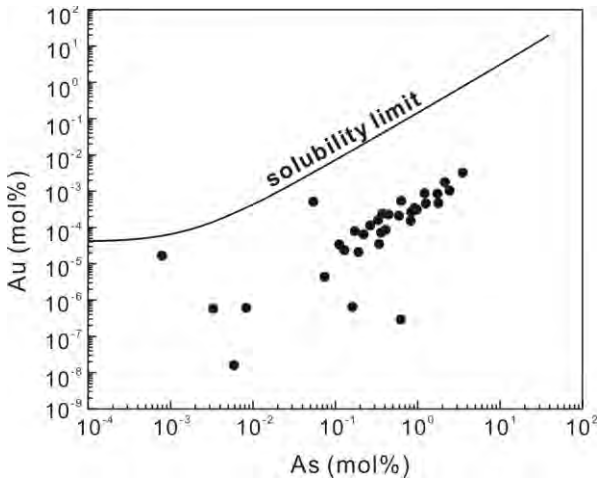

968

This is the peer-reviewed, final accepted version for American Mineralogist, published by the Mineralogical Society of America.
The published version is subject to change. Cite as Authors (Year) Title. American Mineralogist, in press.
DOI: https://doi.org/10.2138/am-2021-7675. http://www.minsocam.org/

969 Figure 5

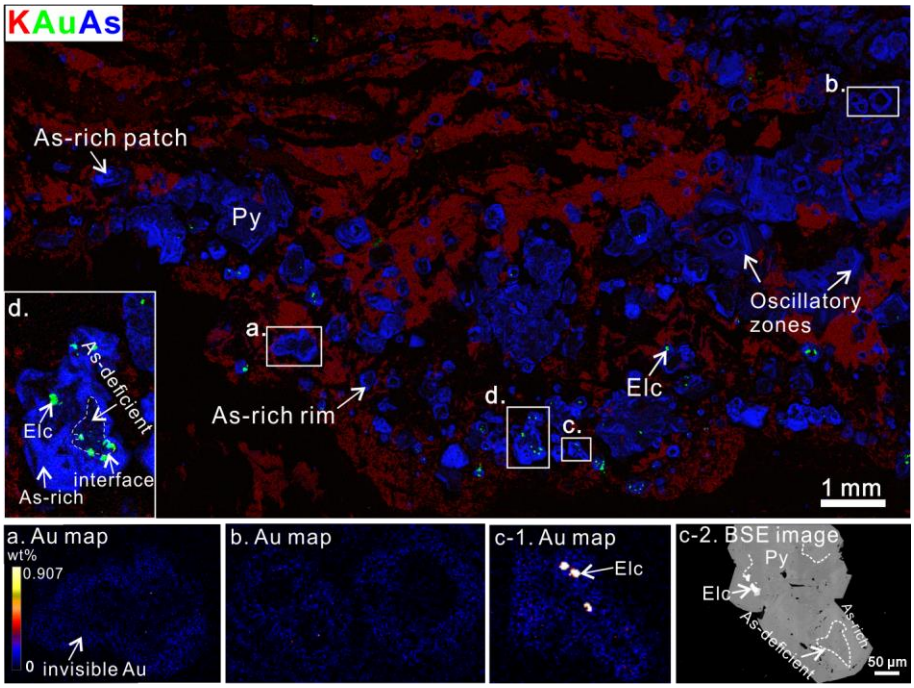

970

971 Figure 6

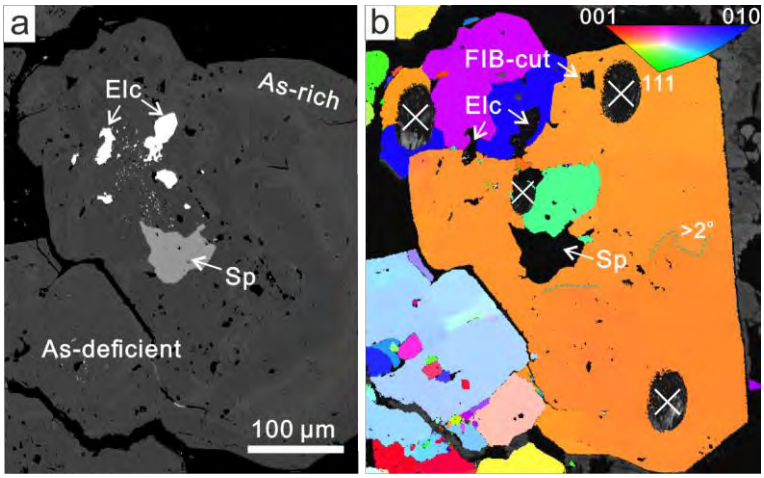

972

973

974 Figure 7

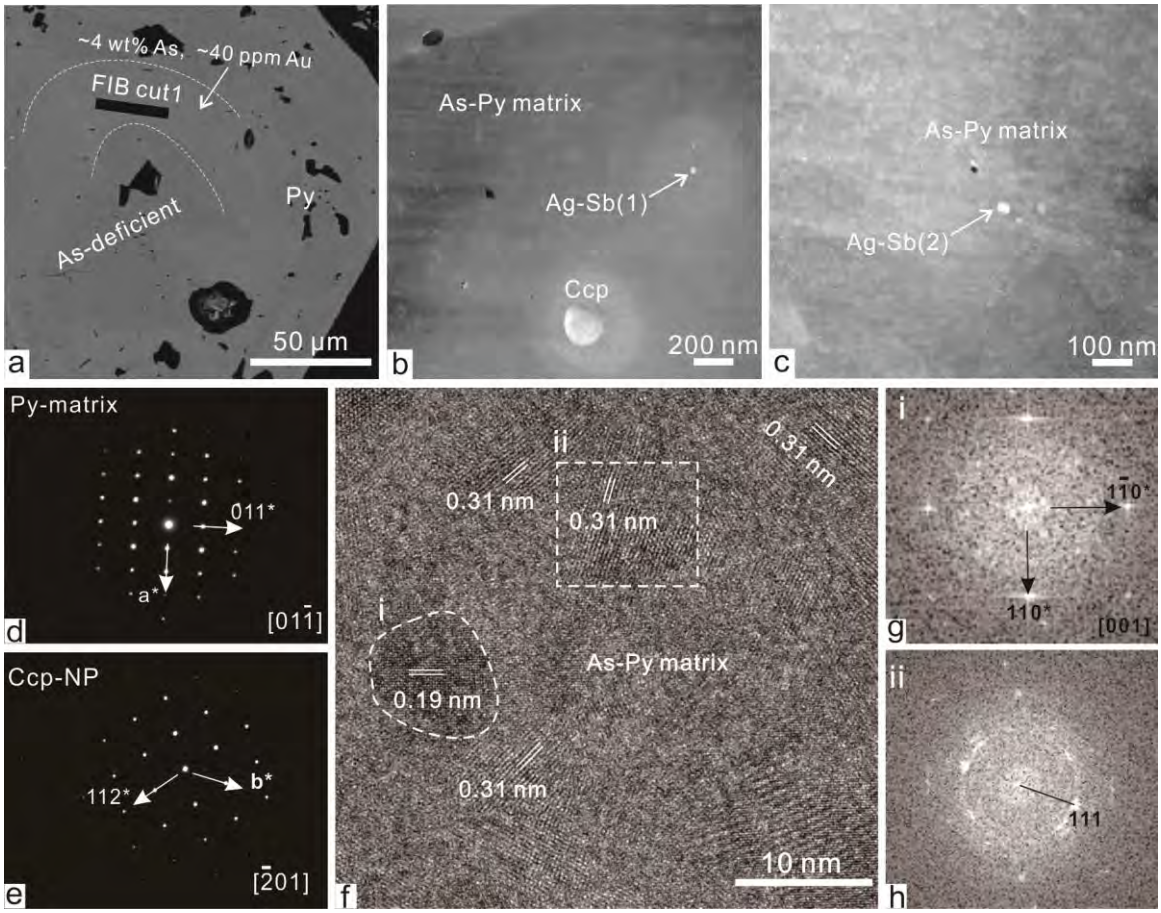

975

976

977 Figure 8

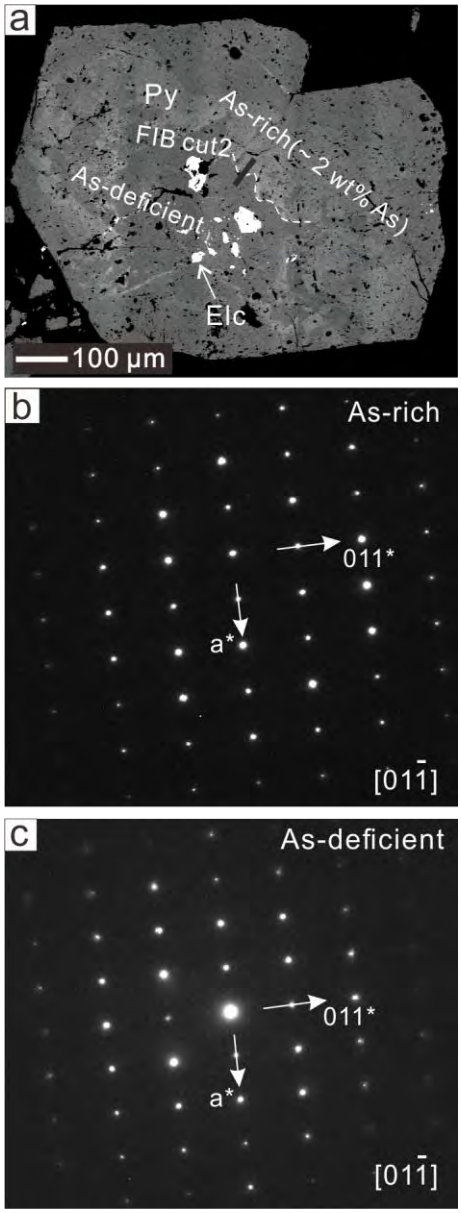

978

979

980 Figure 9

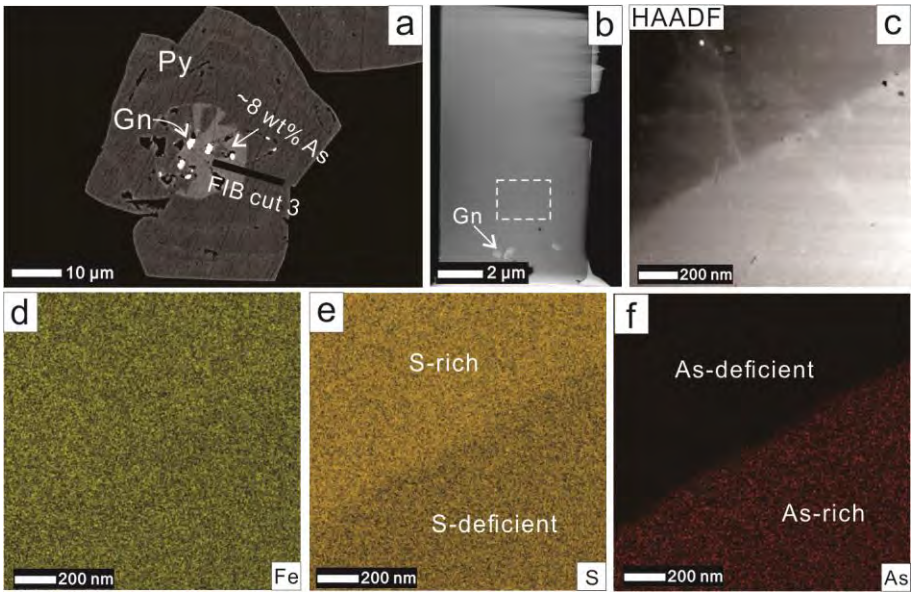

981

982

This is the peer-reviewed, final accepted version for American Mineralogist, published by the Mineralogical Society of America.
The published version is subject to change. Cite as Authors (Year) Title. American Mineralogist, in press.
DOI: https://doi.org/10.2138/am-2021-7675. http://www.minsocam.org/

983 Figure 10

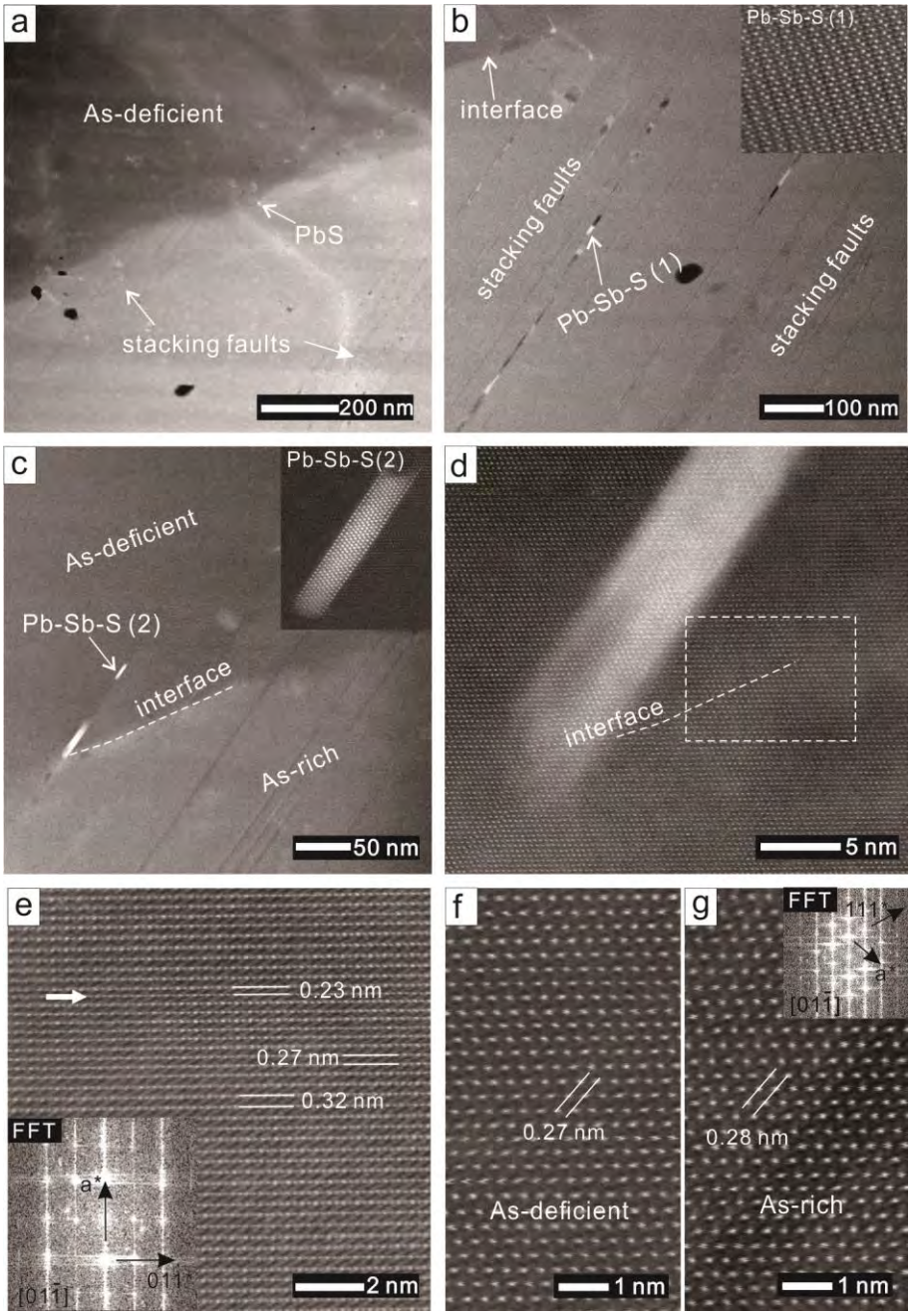

984

985

This is the peer-reviewed, final accepted version for American Mineralogist, published by the Mineralogical Society of America.
The published version is subject to change. Cite as Authors (Year) Title. American Mineralogist, in press.
DOI: https://doi.org/10.2138/am-2021-7675. http://www.minsocam.org/

986 Figure 11

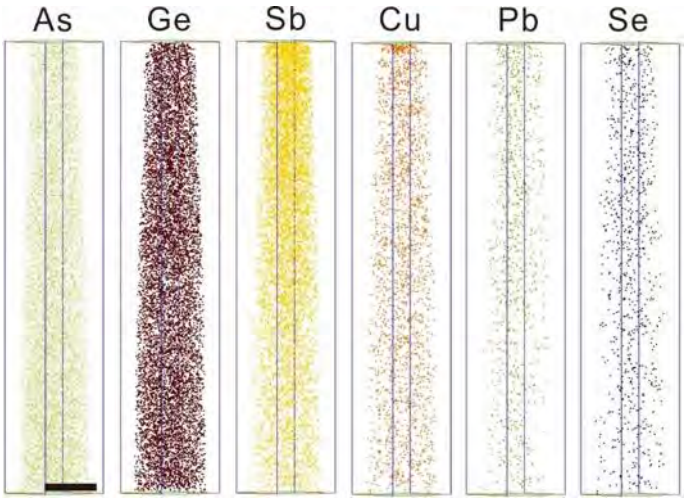

987

988 Figure 12

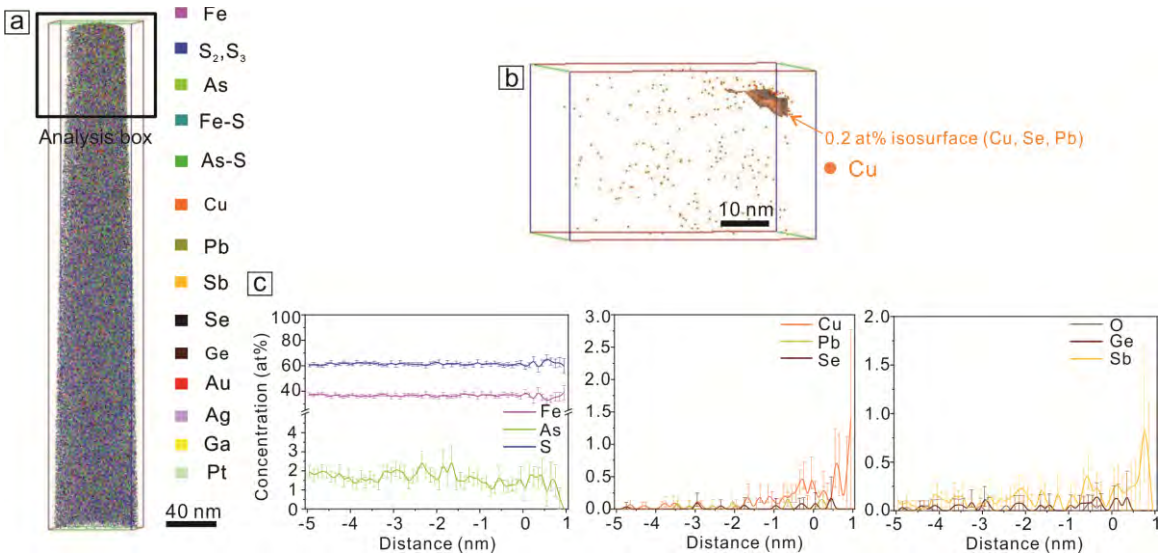

989

990

This is the peer-reviewed, final accepted version for American Mineralogist, published by the Mineralogical Society of America.
The published version is subject to change. Cite as Authors (Year) Title. American Mineralogist, in press.
DOI: https://doi.org/10.2138/am-2021-7675. http://www.minsocam.org/

991 Figure 13

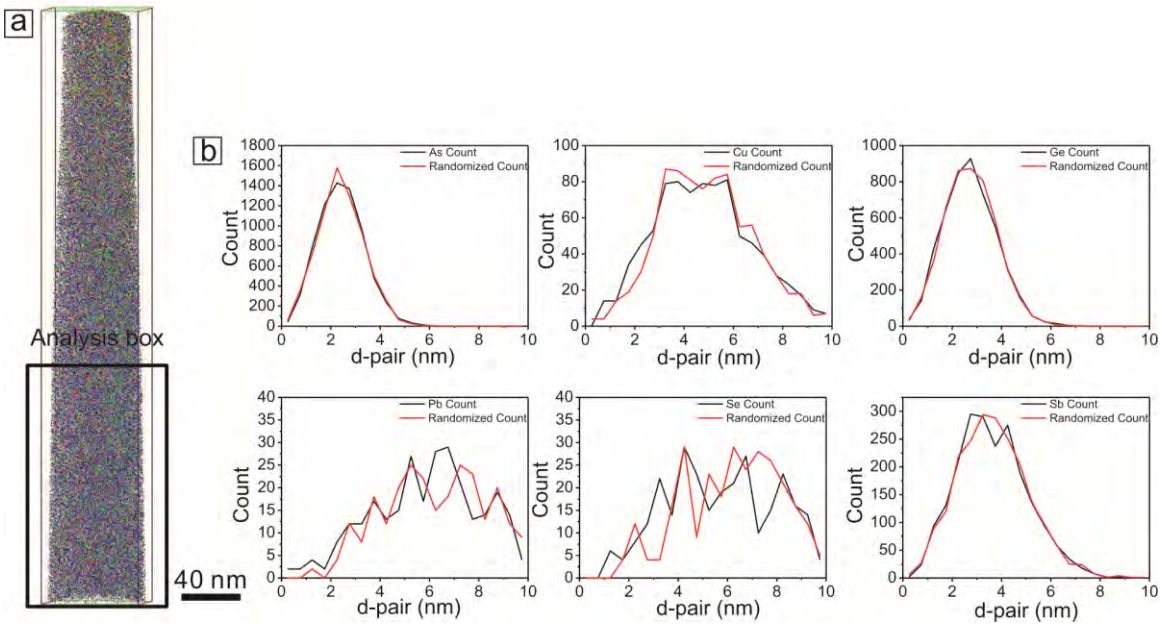

992

993 Figure 14

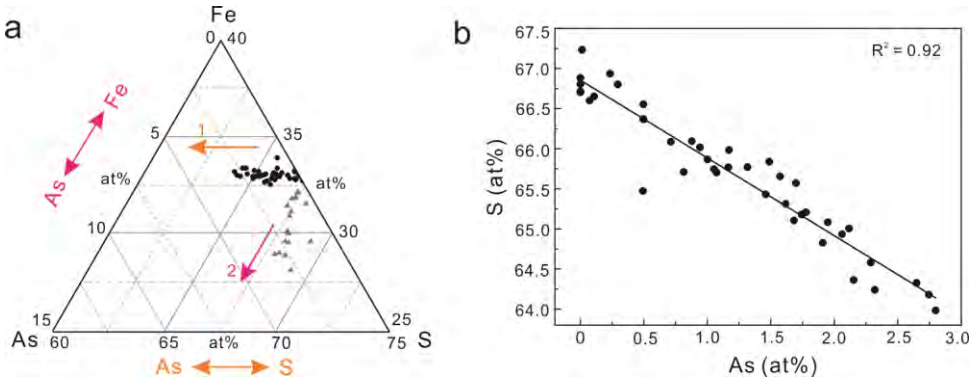

994

995

This is the peer-reviewed, final accepted version for American Mineralogist, published by the Mineralogical Society of America.
The published version is subject to change. Cite as Authors (Year) Title. American Mineralogist, in press.
DOI: https://doi.org/10.2138/am-2021-7675. http://www.minsocam.org/

996 Figure 15

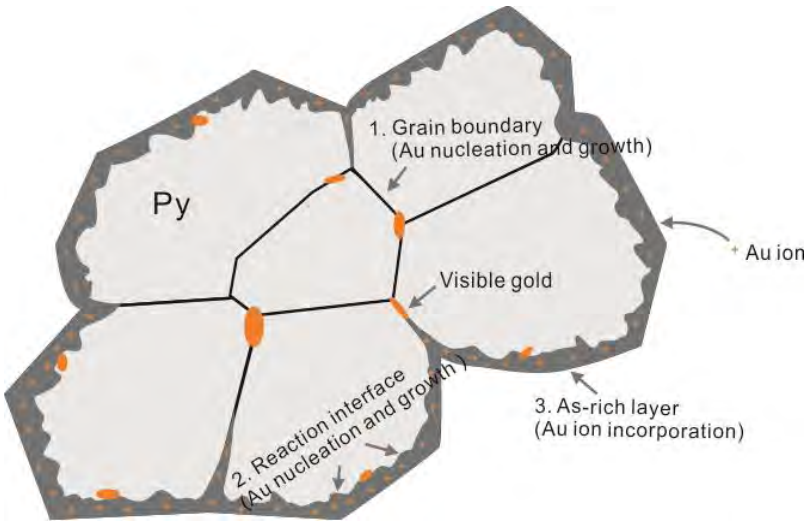

997